Technische Universiteit Delft

Station-keeping in the vicinity of the collinear Lagrange points

MSc Thesis

A.F. Vandenberghe

TU Delft

OHB

Cover image courtesy of OHB System A.G.

Station-keeping in the vicinity of the collinear Lagrange points

MSc Thesis

20/04/2020

by

A.F. Vandenberghe
4274075

Preface

This thesis is the written result of 9 months of research, conducted at OHB System A.G. in Bremen Germany and is written in partial fulfillment for the master in Space Flight at T.U. Delf Aerospace Engineering.

I would like to extend my deepest thanks to the people who have supported me during this period.
First of all my parents, who supported me with love, support and advice.
Secondly, my supervisors, ir. Ron Noomen at T.U. Delft and dr. Javier Herrera at OHB, for their continuous support and advice and for challenging me to find solutions to the multitude of problems that surfaced during this research project.
Finally, my friends and colleagues at OHB and outside, who allowed me to take my mind off this thesis from time to time and for their help when I needed a fresh view on certain things.

A.F. Vandenberghe
Bremen, October 2019

Summary

In this thesis, the performance of three different station-keeping methods applied to Sun-Earth L2 halo orbits was investigated.

In order to evaluate these methods, first a framework for accurate satellite dynamics had to be developed. This was done by starting off at the Circular Restricted Three Body Problem, and extending that to a more accurate model in the Roto-Pulsating Reference Frame (RPF) as described in [1].
The dynamics in the RPF were implemented in a propagator, written in C, which forms the basis for any analysis that has been done for this thesis. The propagator includes real planetary ephemerides from JPL, perturbations from all solar-system bodies and Solar Radiation Pressure and has functionalities for orbit generation, STM propagation, reference frame transformations and manoeuvre calculations.

The three station-keeping methods that have been investigated in this thesis are: Optimal Continuation Strategy (OCS), Discrete-time Sliding Mode Control (DSMC) and Fuzzy-logic Sliding Mode Control (FLSMC). All of these methods were implemented in C, within the developed propagator and were tuned using an optimization library for C (NLOPT [8]).

After the implementation of the three methods, a performance analysis was done, applying the methods to a Sun-Earth L2 halo orbit in a Monte-Carlo simulation, taking into account uncertainties in the orbit determination process, the perturbations and the manoeuvre execution. The total ΔV, as well as the number of manoeuvres, for the three methods were calculated, and subsequently compared against eachother. This was done for a time span of 500 days with a minimum manoeuvre interval of 12 days.

The resulting comparison can be found in Chapter 5 and the result of this analysis clearly shows that the DSMC and FLSMC perform much better both in terms of total ΔV as well as in the variance that arises from the Monte-Carlo simulations. The FLSMC provides another significant, yet smaller, improvement when compared to the DSMC, which was theorized by Lian et al. in [11]. The fuzzy-logic layer that is implemented makes for smoother behaviour when the actual orbit of the satellite is close to the desired reference orbit, where the normal DSMC exhibits more chattering around the reference orbit.
It is clear from this analysis that the proposal of Lian et al. to add this fuzzy logic layer does contribute significantly to the performance of the method and that FLSMC is a potent and efficient method for halo orbit station-keeping, provided a good reference orbit is chosen for the method to follow.

The analysis performed in this thesis was restricted to Sun-Earth L2 halo orbits but all techniques mentioned and developed within this research can easily be applied to halo orbits around any of the collinear lagrange points in any three-body system, with only minor changes.

Contents

List of Symbols

Symbol	Description
A_x	Halo orbit x-amplitude [/]
A_z	Halo orbit z-amplitude [/]
b	Translation vector from an inertial reference frame center to the center of the RPF
C	Rotation matrix from inertial to RPF
$H(\cdot)$	Hamiltonian [/]
J_P	Jerk of the primary body in inertial
J_S	Jerk of the secondary body in inertial
k	Scaling factor from inertial to RPF
$\mathcal{L}(\cdot)$	Lagrangian [/]
M	Monodromy matrix [/]
m_1	Mass of first primary in CRTBP [kg]
m_2	Mass of second primary in CRTBP [kg]
$p.$	Momentum [kg·m/s]
P^n	n-th Legendre Polynomial [/]
R	State in the inertial reference frame
R_P	State of the primary body in inertial
R_S	State of the secondary body in inertial
S_P	Snap of the primary body in inertial
S_S	Snap of the secondary body in inertial
$U(\cdot)$	Potential energy [J]
V_P	Velocity of the primary body in inertial
V_S	Velocity of the secondary body in inertial
$\tilde{U}$	Effective potential [/]
Ω	Gradient of the potential of the n-body problem
ρ	State in the RPF
γ	Unitless distance from Lagrange point to smallest primary [/]
$\eta(\cdot)$	Nominal control in SMC [/]
μ	Mass ratio in CRTBP [/]
$\mu(s)$	Switching function in SMC [/]
σ	Sliding surface in SMC [/]
$\Phi(\cdot)$	State Transition Matrix [/]

List of Abbreviations

Abbreviation	Description
AU	Astronomical Unit
CRTBP	Circular Restricted Three-Body Problem
DC	Differential Correction
DSMC	Discrete-time Sliding Mode Control
ESA	European Space Agency
FLSMC	Fuzzy Sliding Mode Control
IPOPT	Interior Point Optimizer
L1	First Lagrange point
L2	Second Lagrange point
LPO	Libration point orbit
LQR	Linear Quadratic Regulator
NASA	National Aeronautics and Space Administration
NLopt	Non-Linear optimizer
OCS	Optimal Continuation Strategy
ODE	Ordinary Differential Equation
PLATO	PLAnetary Transits and Oscillations of stars
RPF	Roto-Pulsating Reference Frame
SMC	Sliding Mode Control
SRP	Solar Radiation Pressure
SSB	Solar System Barycenter
STM	State Transition Matrix

1 Introduction

Lagrange points and orbits around them are experiencing an increase in interest as new missions are being developed that aim to take advantage of the many interesting properties that Lagrange point orbits exhibit.
The L2-point of the Sun-Earth system is a point that particularly shows interesting qualities for scientific missions. The stable thermal environment, the long-period orbits, the lack of major perturbations and the constant direction with respect to the Sun and the Earth make it a suitable point for space-based telescopes, such as the James Webb or Plato telescope. These telescopes are able to observe the same location for long-periods of time without the Sun or Earth passing their field of view and thus obstructing the measurements.
Halo orbits are a special family of orbits around the collinear Lagrange points that achieve these desirable properties and are relatively stable, provided regular small manoeuvres are made. These station-keeping manoeuvres are required to achieve a periodic and stable orbit and are therefore a vital part of the mission design for Halo orbits.
In this thesis, three different methods for station-keeping in Sun-Earth L2 Halo orbits are analyzed and compared against each other. An efficient station-keeping method can reduce the propellant needed and thus reduce the satellite mass, and can increase the maximum interval between manoeuvres, meaning that in between manoeuvres, longer periods of observations are possible. Both a reduction in required propellant mass and an increase in observation time have a significant impact on the scientific value of these missions and are therefore vital to their success.

First, an introduction is given to the Circular Restricted Three-body Problem (CRTBP) and the theory behind halo orbits. After this, the extension is made from the CRTBP to a more accurate model of satellite dynamics in such a halo orbit, including actual planetary ephemerides, perturbations from other solar-system bodies and solar radiation pressure.

After the development of this framework is explained, the three different station-keeping methods are shown. The first of these methods, Optimal Continuation Strategy (OCS), is a method that is based on certain dynamical properties of halo orbits. The second and third methods are a Discrete-Time Sliding Mode Controller (DSMC) and a Fuzzy-Logic Sliding Mode Controller (FLSMC). These two methods rely on a reference orbit to follow, so the first step in the explanation of these methods is the development of the reference orbit. FLSMC is an addition onto the DSMC method, where fuzzy logic is introduced to improve the behaviour of the method when the satellite is close to the reference orbit.

Finally, the three different methods are compared to each other and their sensitivity to different uncertainties is investigated. All methods are applied to the same Sun-Earth L2 halo orbit and are subjected to a Monte-Carlo analysis taking into account among others orbit determination uncertainties and manoeuvre execution errors.

2

Libration point orbits

The Lagrange points of three-body systems in the solar system possess many interesting properties for space missions and after the first mission to visit one of these points, NASA's International Sun-Earth Explorer 3 to the Sun-Earth L1 point, many have followed suit.
In order to establish why exactly these missions chose a Lagrange point orbit (LPO), a few of their interesting properties are highlighted here in this chapter.
Since this thesis focuses on the Sun-Earth L2 point, this will also be the point discussed here. Together with the Earth-Moon L2 point, this is the Lagrange point that has experienced the most interest due to the characteristics listed below. The theory behind the dynamics at Lagrange point orbits and the Circular Restricted Three-body Problem will be explained in Chapter 3

2.1. Halo orbits

Halo orbits are periodic orbits around one of the collinear Lagrange points, L1, L2 or L3. These orbits exist in any system of two bodies. In the Solar System, the Sun-Earth and the Earth-Moon systems are of particular interest. Missions have been flown in halo orbits in both systems. Halo orbits exhibit multiple interesting properties which can benefit space missions. Among these properties are the following:

- **A stable thermal environment:** The location of these orbits makes its possible to avoid eclipses entirely. This leads to little change in the radiation levels experienced by the spacecraft. This stable thermal environment has positive impacts on measuring equipment and makes the thermal design less constraining.

- **Ability to perform long uninterrupted observations of the same target:** Due to the long periods of Halo orbits, a spacecraft can continuously observe the same part of the sky for much longer than spacecraft in Earth orbits. For spacecraft in a Sun-Earth L2-halo orbit, this observation can be made while completely avoiding interfering radiation coming from the Sun and the Earth, making this location particularly suitable for space-based observatories.

- **Low station-keeping budgets:** Although halo orbits are inherently unstable, the required propellant to keep spacecraft in a stable orbit is very small. The divergence due to the instability can easily be counteracted by performing periodic small station-keeping manoeuvres. The low station-keeping budgets make it possible to design missions with a lifespan of multiple years.

The properties listed above are some of the main reasons why missions have been sent there in the past or are planned to be sent there in the future. Two missions in particular will be highlighted here.

Herschel-Planck: ESA's Herschel-Planck mission consisted of two spacecraft that were launched into different orbits around the Sun-Earth L2 point in 2009. Herschel was an infrared space-based observatory, while Planck was an observatory investigating the cosmic background radiation [6]. Herschel and Planck have reference areas of 23.1 m^2 and 13.8 m^2 respectively, and masses of 2700 kg

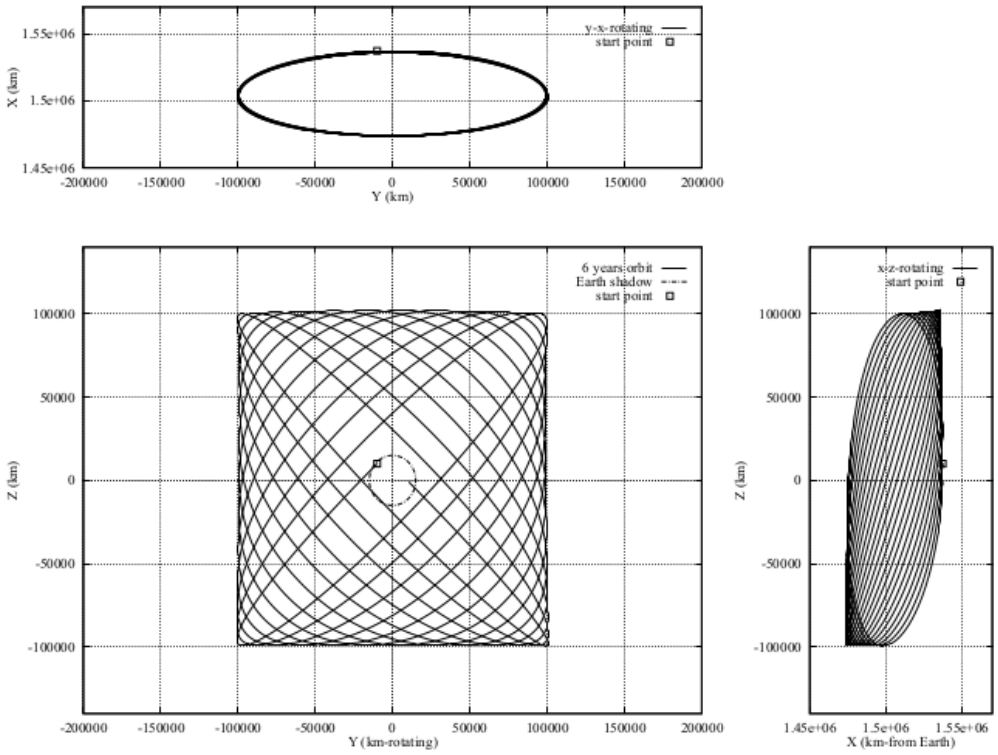

Figure 2.1: Typical Lissajous orbit around Sun-Earth L2 [6].

and 1300 kg respectively.

Orbit: The Herschel satellite was inserted into a Lissajous orbit with an average radius of 800000 km, while Planck was inserted into a Lissajous orbit with an average radius of 400000 km (Figure 2.1).

Manoeuvres: The Herschel and Planck station-keeping manoeuvres were both limited in frequency to one manoeuvre every 30 days and the ΔV-budget reached no more than 1 m/s/yr .

Plato: Plato (Planetary Transits and Oscillations of Stars) is an ESA mission designed to be launched in 2025. Plato will perform measurements in order to detect exoplanets and will do so in a Halo orbit around the Sun-Earth L2 point [3].
This location allows for unhindered observations in one hemisphere as the positions of the Sun and the Earth relative to the satellite remain relatively constant. Plato will have a mass of 2120 kg.

Orbit: The exact parameters of Plato's orbit still remain largely unknown. The specific orbit which will be used depends heavily on the launch date. However, for the definition report, a Halo orbit with a y-amplitude of $8 \cdot 10^5$ km and a z-amplitude of around $5 \cdot 10^5$ km is assumed.

Manoeuvres: Due to the scientific purpose of Plato, which is to detect exoplanets through transit measurements, long uninterrupted measurement periods are required. This leads to a constraint on the minimum interval between subsequent station-keeping manoeuvres of three weeks. Further mission properties remain unknown as of yet but may be acquired during the thesis.

I

Three-Body Dynamics

3

Circular Restricted Three-Body Problem

The Lagrange points are equilibrium points in the CRTBP. This chapter will focus on the CRTBP and the dynamics of Lagrange point orbits in such a CRTBP.

3.1. Principles

The CRTBP is a three-body problem where one body, the satellite, has negligible mass compared to the two primaries. In this thesis, the Sun and the Earth are considered as primary bodies. Furthermore the motion of the primaries around their common barycenter is set to be circular.
The CRTBP is typically studied using a rotating reference frame. This reference frame (shown in Figure 3.1 for the Sun-Earth System) is defined as follows: [10]

- **Origin:** Located at the barycenter of the two primaries.
- **x-axis:** On the line connecting both primaries, positive in the direction of the smaller one of the two.
- **z-axis:** Along the angular momentum vector.
- **y-axis:** Completing the right-hand system.

The units in the CRTBP reference frame are normalized by scaling both the distance between the two primaries and the angular velocity of the two primaries around their barycenter to unity.
With the mass of the two primaries, m_1 and m_2, the mass ratio μ is defined as

$$\mu = \frac{m_2}{m_1 + m_2} \tag{3.1}$$

In a two-dimensional problem formulation, the location of the two primaries is given by $(-\mu, 0)$ and $(1-\mu, 0)$, while the location of the third body is given by (x, y).
Another normalization that is done is setting the mass of the third body to unity. This leads to the following expression for the kinetic energy K of the third body:

$$K(x, y, \dot{x}, \dot{y}) = \frac{1}{2}\left[(\dot{x} - y)^2 + (\dot{y} + x)^2\right] \tag{3.2}$$

As a final simplification, the motion is restricted to the orbital plane of the primaries. This is called the Planar CRTBP. Later on in this chapter, the motion in the z-direction will no longer be restricted and the CRTBP in three dimensions will be discussed.

Using the locations of the two primaries, the distance from the third body to the primaries is given by:

$$r_1 = \sqrt{(x + \mu)^2 + y^2} \tag{3.3}$$

$$r_2 = \sqrt{(x - 1 + \mu)^2 + y^2} \tag{3.4}$$

Using these distances, the specific potential energy of the third body can be described as follows:

$$U(x, y) = -\frac{1 - \mu}{r_1} - \frac{\mu}{r_2} \tag{3.5}$$

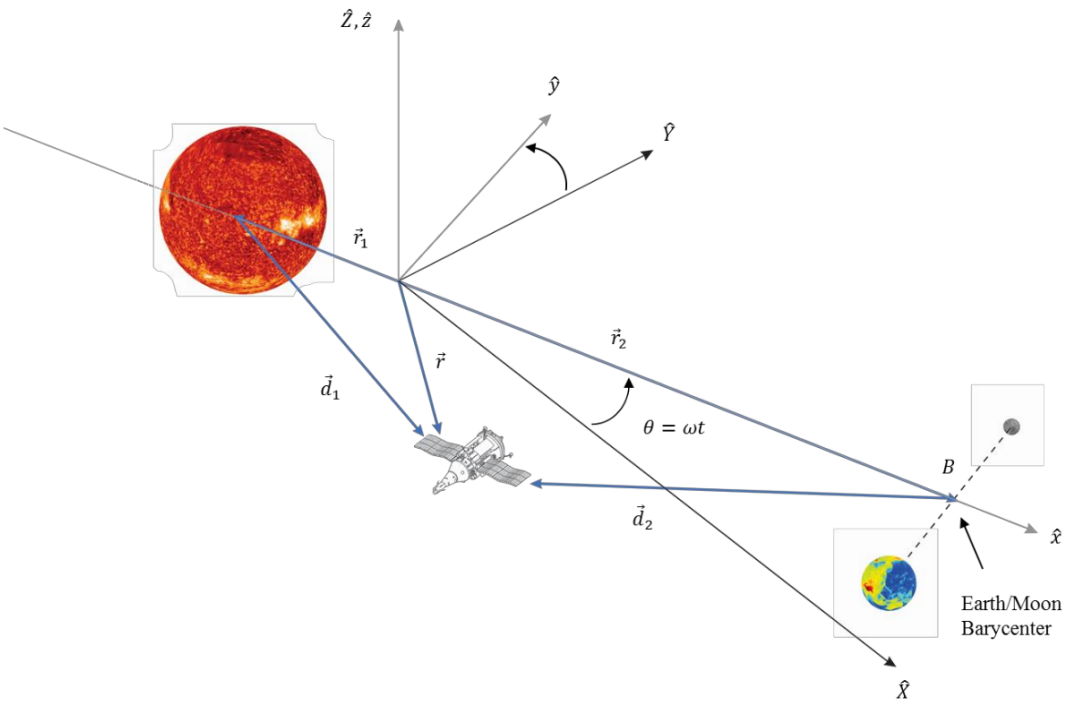

Figure 3.1: Geometry of the Circular Restricted Three Body Problem [15].

In an alternative formulation, the Lagrangian of the third body is given by its kinetic energy minus its potential energy:

$$\mathcal{L}(x, y, \dot{x}, \dot{y}) = K(x, y, \dot{x}, \dot{y}) - U(x, y) \tag{3.6}$$

Using the Euler-Lagrange equations Equation (3.7), the equations of motion of the third body can be obtained.

$$\frac{\delta \mathcal{L}}{\delta q_i}(t, \mathbf{q}(t), \dot{\mathbf{q}}(t)) - \frac{d}{dt}\frac{\delta \mathcal{L}}{\delta \dot{q}_i}(t, \mathbf{q}(t), \dot{\mathbf{q}}(t)) = 0 \quad \text{for i = 1,2} \tag{3.7}$$

where **q** is the position vector and $\dot{\mathbf{q}}$ is the velocity vector.

This leads to the following equations of motion:

$$\ddot{x} - 2\dot{y} = -\frac{\delta \bar{U}}{\delta x} \tag{3.8}$$

$$\ddot{y} + 2\dot{x} = -\frac{\delta \bar{U}}{\delta y} \tag{3.9}$$

In Equations 3.8 and 3.9, $\bar{U}$ is the effective potential, given by Equation (3.10).

$$\bar{U} = U - \frac{x^2 + y^2}{2} = -\frac{1}{2}((1-\mu)r_1^2 + \mu r_2^2) - \frac{1-\mu}{r_1} - \frac{\mu}{r_2} \tag{3.10}$$

Using the Legendre Transform, the conserved energy can be calculated to be:

$$E = \frac{1}{2}(\dot{x}^2 + \dot{y}^2) + \bar{U}(x, y) \tag{3.11}$$

3.2. Lagrange points

The Lagrange points in the CRTBP are defined as points where the third body is stationary in the CRTBP reference frame. This leads to circular orbits with the same period as the orbit of the primaries around the barycentre.

From Equations 3.8 and 3.9, it is clear that these equilibria occur at the critical points of the effective potential $\bar{U}$, where the partial derivative is zero. These critical points occur at the locations shown in Figure 3.2.

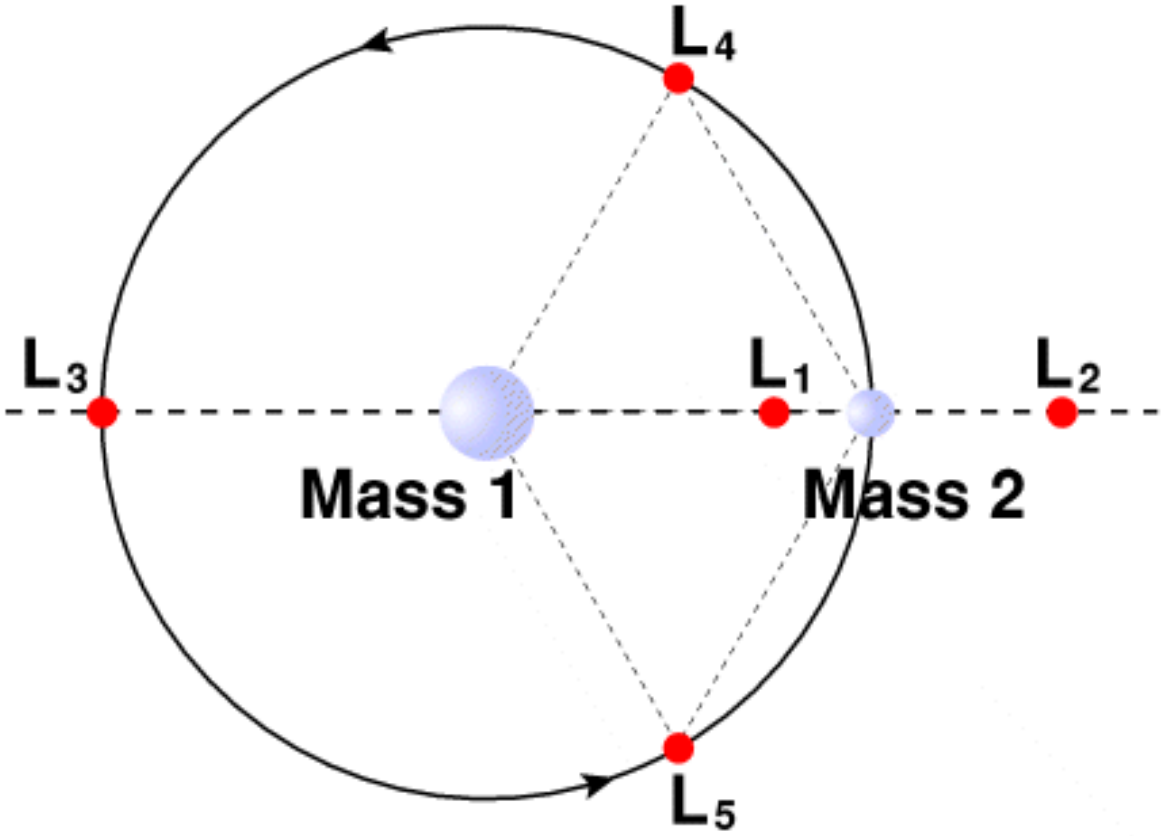

Figure 3.2: Location of the Lagrange points (NASA)

3.2.1. Motion near Lagrange points

The motion near the Lagrange points can be described by developing linearized equations of motion around these equilibria. This will be done using the Hamiltonian formulation of the equations of motion. Starting from the Lagrangian described in Equation (3.6), the Hamiltonian form can be obtained by performing the Legendre transformation:

$$\dot{q}^i = \frac{\delta \mathcal{L}}{\delta q^i}; \qquad H(q^i, p_i) = \sum_{i=1}^{n} p_i \dot{q}^i - \mathcal{L}(q^i, p_i) \tag{3.12}$$

The Hamiltonian equations are in the form of:

$$\dot{q}^i = \frac{\delta H}{\delta p_i}; \qquad \dot{p}_i = -\frac{\delta H}{\delta q^i} \tag{3.13}$$

The Legendre transform is given here by: [10]

$$\begin{aligned} p_x &= \frac{\delta \mathcal{L}}{\delta \dot{x}} = \dot{x} - y \\ p_y &= \frac{\delta \mathcal{L}}{\delta \dot{y}} = \dot{y} + x \end{aligned} \tag{3.14}$$

The Hamiltonian function $H(x, y, p_x, p_y)$ is then obtained as:

$$\begin{aligned} H(x, y, p_x, p_y) &= p_x\dot{x} + p_y\dot{y} - \mathcal{L} \\ &= \frac{1}{2}((p_x + y)^2 + (p_y - x)^2) + \bar{U} \end{aligned} \tag{3.15}$$

The Hamiltonian equations of motion are now given by:

$$\begin{aligned} \dot{x} &= \frac{\delta H}{\delta p_x} = p_x + y \\ \dot{y} &= \frac{\delta H}{\delta p_y} = p_y - x \\ \dot{p_x} &= -\frac{\delta H}{\delta x} = p_y - x - \bar{U}_x \\ \dot{p_y} &= -\frac{\delta H}{\delta y} = -p_x - y - \bar{U}_y \end{aligned} \tag{3.16}$$

The equations of motion from Equation (3.16) are then linearized around the equilibria $(x_e, y_e, \dot{x}_e, \dot{y}_e) = (x_e, 0, 0, 0)$ or in the Hamiltonian system $(x_e, y_e, p_x, p_y) = (x_e, 0, 0, x_e)$. By applying a transformation to shift the origin of the reference frame to these equilibria the following expressions arise:

$$H = \frac{1}{2}\left[(p_x + y)^2 + (p_y - x)^2 - ax^2 + by^2\right] \tag{3.17}$$

with $a = 2 \cdot \bar{\mu} + 1$, and $b = \bar{\mu} - 1$ and

$$\bar{\mu} = \mu|x_e - 1 + \mu|^{-3} + (1 - \mu)|x_e + \mu|^{-3} \tag{3.18}$$

.

$$\begin{aligned} \dot{x} &= \frac{\delta H}{\delta p_x} = p_x + y \\ \dot{y} &= \frac{\delta H}{\delta p_y} = p_y - x \\ \dot{p_x} &= -\frac{\delta H}{\delta x} = p_y - x + ax \\ \dot{p_y} &= -\frac{\delta H}{\delta y} = -p_x - y - by \end{aligned} \tag{3.19}$$

This gives the following matrix form of the equations Equation (3.20), which will be used to demonstrate the stability of the equilibria.

$$\begin{bmatrix} \dot{x} \\ \dot{y} \\ \dot{v}_x \\ \dot{v}_y \end{bmatrix} = \begin{bmatrix} 0 & 0 & 1 & 0 \\ 0 & 0 & 0 & 1 \\ a & 0 & 0 & 2 \\ 0 & -b & -2 & 0 \end{bmatrix} \begin{bmatrix} x \\ y \\ v_x \\ v_y \end{bmatrix} = A \begin{bmatrix} x \\ y \\ v_x \\ v_y \end{bmatrix} \tag{3.20}$$

The characteristic equation of matrix A will be solved to get the eigenvalues of the system. From the eigenvalues, the stability of the system can be derived.

$$p(\beta) = \beta^4 + (2 - \bar{\mu})\beta^2 + (1 + \bar{\mu} - 2\bar{\mu}^2) \tag{3.21}$$

Let $\alpha = \beta^2$:

$$p(\alpha) = \alpha^2 + (2 - \bar{\mu})\alpha + (1 + \bar{\mu} - 2\bar{\mu}^2) \tag{3.22}$$

The two solutions for α are then:

$$\begin{aligned} \alpha_1 &= \frac{\bar{\mu} - 2 + \sqrt{9\bar{\mu}^2 - 8\bar{\mu}}}{2} \\ \alpha_2 &= \frac{\bar{\mu} - 2 - \sqrt{9\bar{\mu}^2 - 8\bar{\mu}}}{2} \end{aligned} \tag{3.23}$$

The last term of $p(\beta)$ is equal to $-ab$. This term is negative, making the quadratic equation for $p(\alpha)$ have one positive and one negative root. The eigenvalues β will therefore be of the following form.

$$\begin{aligned} \beta_1 &= +\lambda \\ \beta_2 &= -\lambda \\ \beta_3 &= +iv \\ \beta_4 &= -iv \end{aligned} \tag{3.24}$$

The existence of the non-negative real eigenvalues at the equilibria proves the unstability of the collinear Lagrange points.

3.3. Construction of libration point orbits

Although the collinear Lagrange points are inherently unstable, families of periodic orbits around these points still exist. However, due to the unstability discussed above, these orbits diverge quickly and therefore require station-keeping.

The main families of orbits are:

- Lyapunov orbits: Periodic orbits in the plane of the two primary bodies
- Lissajous orbits: Quasi-periodic orbits with an out-of-plane component
- Halo orbits: Periodic orbits with an out-of-plane component
- Quasi-Halo orbits: Quasi-periodic orbits situated on a torus around a Halo orbit

This thesis will focus on the Halo orbit family and more specifically on Halo orbits around the Sun-Earth L2, although the same methods can easily be used without much adaptation to construct Halo orbits around L1.

3.3.1. Dynamics

The equations of motion in the planar CRTBP (Equations 3.8 and 3.9), near the collinear Lagrange points, are extended to the spatial problem by adding the equation of motion of the out-of-plane component.

$$\begin{aligned} \ddot{x} - 2\dot{y} &= -\bar{U}_x \\ \ddot{y} + 2\dot{x} &= -\bar{U}_y \\ \ddot{z} &= -\bar{U}_z \end{aligned} \tag{3.25}$$

These equations are once again centered around the Lagrange point and normalized by applying the following coordinate transformation:

$$\begin{aligned} \bar{x} &= \frac{x - 1 + \mu \pm \gamma}{\gamma} \\ \bar{y} &= \frac{y}{\gamma} \\ \bar{z} &= \frac{z}{\gamma} \end{aligned} \tag{3.26}$$

In Equation (3.26), γ is the distance from the libration point to the smallest primary, the $+$-sign corresponds to L1, while the $-$-sign corresponds to L2. This normalized coordinate system is scaled

so that the distance between either L1 or L2 and the primary body is equal to the unit length.
After this coordinate transformation, the equations of motion, Equation (3.25), are expanded using Legendre polynomials. The right-hand side of the equations of motion contain the potential $\bar{U}$, which has nonlinear terms $\frac{1-\mu}{r_1}$ and $\frac{\mu}{r_2}$. These can be expanded using the following identity.

$$\frac{1}{\sqrt{(x-A)^2+(y-B)^2+(z-C)^2}} = \frac{1}{D}\sum_{n=0}^{\infty}\left(\frac{\rho}{D}\right)^n P_n\left(\frac{Ax+By+Cz}{D\rho}\right) \tag{3.27}$$

with $D^2 = A^2 + B^2 + C^2$ and $\rho = x^2 + y^2 + z^2$.
The equations of motion Equation (3.25) can be expanded using Legendre Polynomials as follows:

$$\begin{aligned}
\ddot{x} - 2\dot{y} - (1+2c_2)x &= \frac{\delta}{\delta x}\sum_{n=0}^{n\leq 3} c_n \rho^n P_n\left(\frac{x}{\rho}\right) \\
\ddot{y} + 2\dot{x} + (c_2 - 1)y &= \frac{\delta}{\delta y}\sum_{n=0}^{n\leq 3} c_n \rho^n P_n\left(\frac{x}{\rho}\right) \\
\ddot{z} + c_2 z &= \frac{\delta}{\delta z}\sum_{n=0}^{n\leq 3} c_n \rho^n P_n\left(\frac{x}{\rho}\right)
\end{aligned} \tag{3.28}$$

where

$$c_n = \frac{1}{\gamma^3}\left((\pm 1)^n \mu + (-1)^n \frac{(1-\mu)\gamma^{n+1}}{(1 \mp \gamma)^{n+1}}\right) \tag{3.29}$$

In Equation (3.29), the upper sign in the $\pm$ and $\mp$ corresponds to L1, while the lower sign corresponds to L2.

3.3.2. Solutions

Firstly, the non-linear equations in Equation (3.28) are linearized and periodic solutions for these linear equations are developed. In the next subsection, a method is shown to obtain approximate periodic solutions of the non-linear equations.

The linear part of the equations of motion can be obtained by setting the right-hand side of Equation (3.28) to zero.

$$\begin{aligned}
\ddot{x} - 2\dot{y} - (1+2c_2)x &= 0 \\
\ddot{y} + 2\dot{x} + (c_2 - 1)y &= 0 \\
\ddot{z} + c_2 z &= 0
\end{aligned} \tag{3.30}$$

It is clear from Equation (3.30) that the out-of-plane solution is harmonic since $c_2 > 0$. This component is independent from the motion in the xy-plane. The two other components are however coupled. With the addition of the out-of-plane motion, two more eigenvalues are added to those shown in Section 3.2.1. The eigenvalues of the system become $(\pm\lambda, \pm i\omega_p, \pm i\omega_v)$, with:

$$\begin{aligned}
\lambda^2 &= \frac{c_2 + \sqrt{9c_2^2 - 8c_2}}{2} \\
\omega_p^2 &= \frac{2 - c_2 + \sqrt{9c_2^2 - 8c_2}}{2} \\
\omega_v^2 &= c_2
\end{aligned} \tag{3.31}$$

Since λ_1 and λ_2 are opposite in sign, the system will in general be unbounded. The initial conditions however can be restricted so that the divergence in the system is eliminated. This will lead to a periodic solution in xy. Applying these restrictions leads to the following solution for the linearized system:

$$\begin{aligned} x &= -A_x \cos(\omega_p t + \Phi) \\ y &= \kappa A_x \sin(\omega_p t + \Phi) \\ z &= A_z \sin(\omega_v t + \phi) \end{aligned} \tag{3.32}$$

with:

$$\kappa = \frac{\omega_p^2 + 1 + 2c_2}{2\omega_p} = \frac{2\lambda}{\lambda^2 + 1 - c_2} \tag{3.33}$$

In literature, two constraints have been identified specifically for Halo orbits. This was done using perturbation analysis [5].

Amplitude Constraint

Any Halo orbit can be fully defined by specifying an out-of-plane amplitude A_z. The following relation can then be used to identify the amplitude in the x-direction.

$$l_1 A_x^2 + l_2 A_z^2 + \Delta = 0 \tag{3.34}$$

The coefficients l_1, l_2 and Δ are specific to the primary and secondary bodies and to the Lagrange point around which the orbit is situated.
For the Sun-Earth system, the following values for these coefficients have been found [10]:

	L_1	L_2
l_1	-1.596	-1.482
l_2	1.740	1.674
Δ	0.292	0.291

Table 3.1: Amplitude constraint coefficients Sun-Earth System.

Phase-angle Relationship

The phases Φ and ϕ for Halo orbits are related to each other by the following expression:

$$\phi - \Phi = m\pi/2, \qquad m = 1, 3 \tag{3.35}$$

The two options for m in this relationship result in two families of Halo orbits. Setting $m = 1$ leads to a Northern Halo orbit, which reaches the maximum distance from the orbital plane of the two primaries in the positive z-direction, while setting $m = 3$ leads to a Southern Halo orbit, which reaches its maximum distance from the orbital plane of the two primaries in the negative z-direction.
Families of Northern and Southern Halo Orbits around the Earth-Moon L1 point are shown in Figures 3.3 and 3.4, respectively.

3.3.3. Third-order Richardson Expansion

Richardson [12] developed an approximate method to construct periodic solutions of the non-linear equations of motion. This solution will use the 3rd-order Legendre polynomial terms from the equations of motion described in Equation (3.28). The corresponding equations of motion for the approximation are then:

$$\begin{aligned} \ddot{x} - 2\dot{y} - (1 + 2c_2)x &= \frac{3}{2}c_3(2x^2 - y^2 - z^2) + 2c_4 x(2x^2 - 3y^2 - 3z^2) + O(4) \\ \ddot{y} + 2\dot{x} + (c_2 - 1)y &= -3c_3 xy - \frac{3}{2}c_4 y(4x^2 - y^2 - z^2) + O(4) \\ \ddot{z} + c_2 z &= -3c_3 xz - \frac{3}{2}c_4 z(4x^2 - y^2 - z^2) + O(4) \end{aligned} \tag{3.36}$$

The Halo periodic solutions are obtained by assuming large enough amplitudes A_x and A_z of the linearized solution, which leads to the two eigenfrequencies ω_p and ω_v being equal to each other.

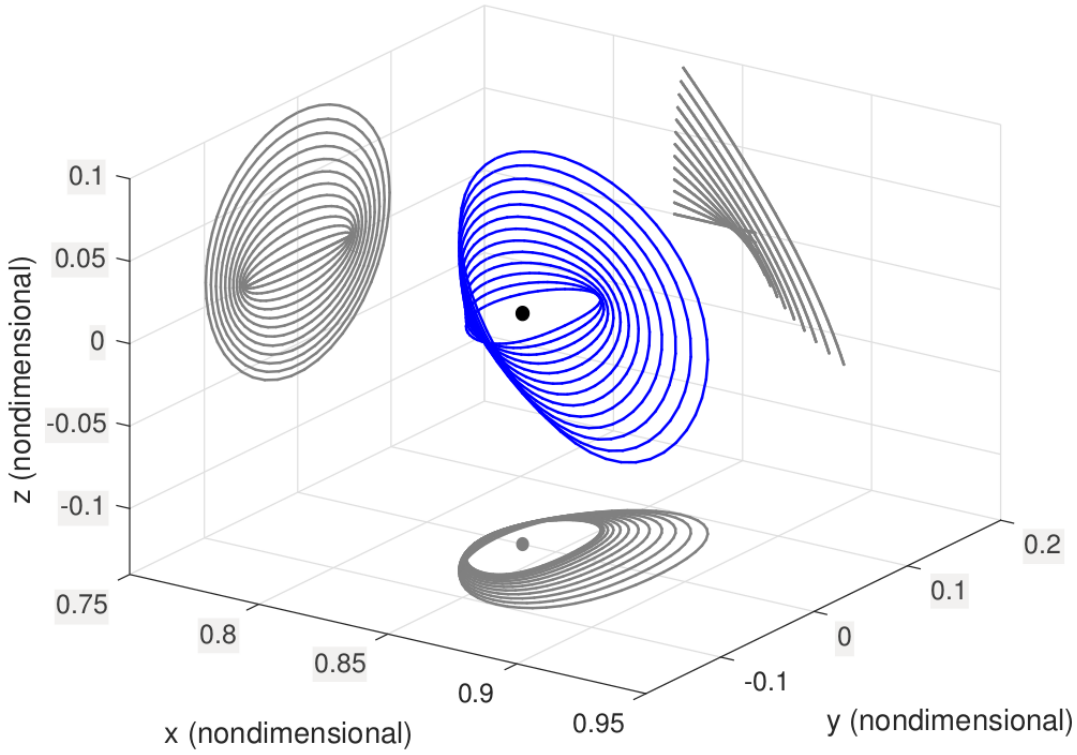

Figure 3.3: Family of Earth–Moon L1 Northern Halo Orbits with projections on the coordinate planes; the black dot and its gray projection denote the L1 point. [14]

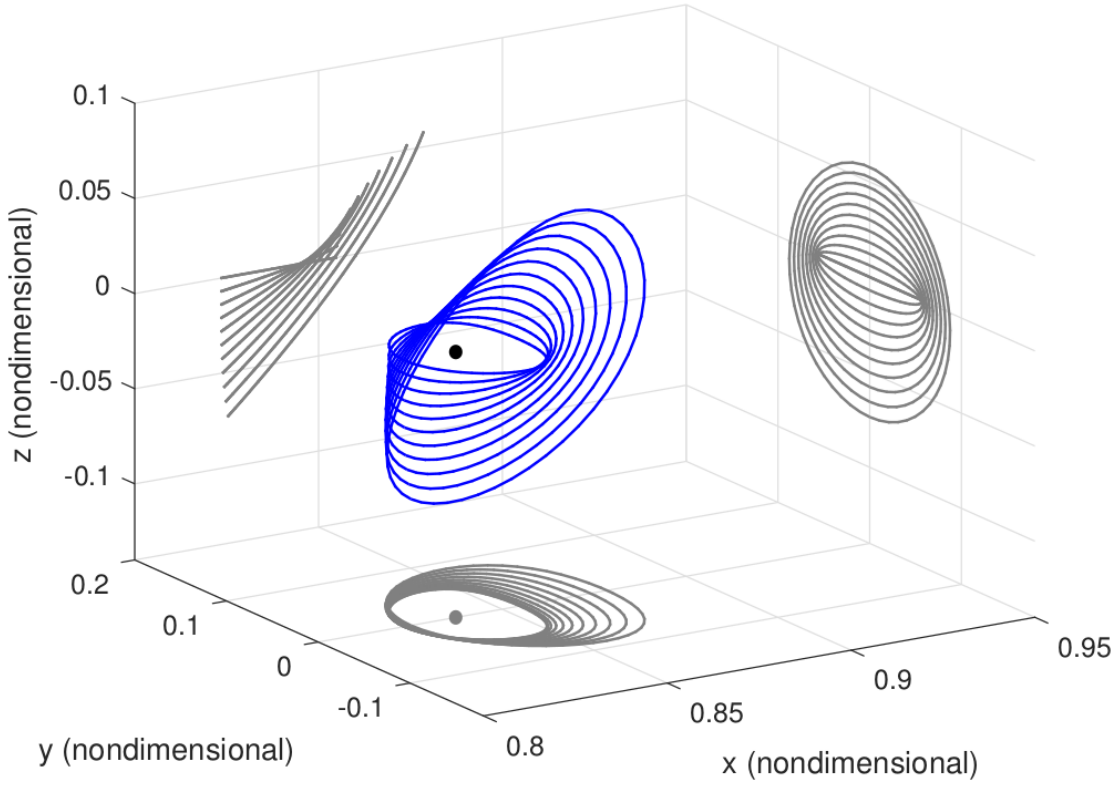

Figure 3.4: Family of Earth–Moon L1 Southern Halo Orbits with projections on the coordinate planes; the black dot and its gray projection denote the L1 point. [14]

The linearized equations in Equation (3.30) can then be rewritten as follows:

$$\begin{aligned} \ddot{x} - 2\dot{y} - (1 + 2\omega_p^2)x &= 0 \\ \ddot{y} + 2\dot{x} + (\omega_p^2 - 1)y &= 0 \\ \ddot{z} + \omega_p^2 z &= 0 \end{aligned} \tag{3.37}$$

which have the following periodic solution:

$$\begin{aligned} x &= -A_x \cos(\omega_p t + \Phi) \\ y &= \kappa A_x \sin(\omega_p t + \Phi) \\ z &= A_z \sin(\omega_p t + \phi) \end{aligned} \tag{3.38}$$

Correction term for out-of-plane component

Imposing this restriction for the out-of-plane component makes it necessary to add an extra correction term to the right-hand side of the equation of motion for z:

$$\Delta = \omega_p^2 - c_2 = \omega_p^2 - \omega_v^2 \tag{3.39}$$

The z-equation then becomes

$$\ddot{z} + \omega_p^2 z = -3c_3 xz - \frac{3}{2}c_4 z(4x^2 - y^2 - z^2) + \Delta \cdot z + O(4) \tag{3.40}$$

Lindstedt-Poincaré method

The Lindstedt-Poincaré method is a technique used in perturbation theory to approximate periodic solutions to ordinary differential equations. The goal of the method is to remove secular terms, which leads to a periodic solution.

A new independent variable τ and a frequency connection ν are introduced using

$$\tau = \nu t \tag{3.41}$$

with

$$\nu = 1 + \sum_{n \leq 1} \nu_n, \qquad \nu_n < 1 \tag{3.42}$$

The ν_n are specifically chosen to eliminate secular terms and arrive at the periodic solution.
The equations of motion rewritten in terms of the new independent variable τ become

$$\begin{aligned} \nu^2 x'' - 2\nu y' - (1 + 2c_2)x &= \frac{3}{2}c_3(2x^2 - y^2 - z^2) + 2c_4 x(2x^2 - 3y^2 - 3z^2) + O(4) \\ \nu^2 y'' + 2\nu x' + (c_2 - 1)y &= -3c_3 xy - \frac{3}{2}c_4 y(4x^2 - y^2 - z^2) + O(4) \\ \nu^2 z'' + \omega_p^2 z &= -3c_3 xz - \frac{3}{2}c_4 z(4x^2 - y^2 - z^2) + \Delta \cdot z + O(4) \end{aligned} \tag{3.43}$$

Third-order Richardson method

The solution for periodic Halo orbits using the third-order Richardson method is given by Equation (3.44):

$$\begin{aligned} x &= a_{21}A_x^2 + a_{22}A_z^2 - A_x \cos\tau_1 + (a_{23}A_x^2 - a24A_z^2)\cos 2\tau_1 + (a_{31}A_x^2 - a_{32}A_x A_z^2)\cos 3\tau_1 \\ y &= \kappa A_x \sin\tau_1 + (b_{21}A_x^2 - b_{22}A_z^2)\sin 2\tau_1 + (b_{31}A_x^3 - b_{32}A_x A_z^2)\sin 3\tau_1 \\ z &= \delta_m A_z \cos\tau_1 + \delta_m d_{21}A_x A_z(\cos 2\tau_1 - 3) + \delta_m(d_{32}A_z A_x^2 - d_{31}A_z^3)\cos 3\tau_1 \end{aligned} \tag{3.44}$$

The expressions for all the coefficients used in Equation (3.44) can be found in Appendix A.

3.3.4. Numerical construction of Halo orbits

In order to create numerical solutions of periodic Halo orbits, the third-order Richardson expansion shown in Section 3.3.3 can be used as an initial guess. The Richardson expansion solutions are given with respect to the Lagrange point in question. If the desired solution is to be given centered in the largest primary body, the translation of the origin will magnify the errors introduced by the truncation at 3rd order. In order to maintain a periodic orbit in the new reference frame, a differential correction can be made to correct the initial conditions.

In order to achieve this, the state transition matrix has to be propagated alongside the state of the satellite. This state transition matrix can then be used to change the initial values, making use of the fact that a periodic Halo orbit will cross the xz-plane in a perpendicular fashion. Thus, when starting with initial conditions at one perpendicular crossing of the xz-plane, $\bar{x}_0 = (x_0, 0, z_0, 0, \dot{y}_0, 0)^T$, after propagating for one half of the period of the orbit, the final state $\bar{x}_f$ should be of the form $\bar{x}_f = (x_f, 0, z_f, 0, \dot{y}_f, 0)^T$. Using the state transition matrix, the initial state is then iteratively updated until the velocity components in the x and z-direction are sufficiently close to zero. This process is then repeated where the STM is propagated one plane crossing further. The halo orbit resulting from this process will be used as initial conditions for halo orbit generation in the full solar system model in the next chapter. The process of differential correction is further explained in Section 6.0.1, as it is an important part of one of the station-keeping methods analyzed in this thesis.

4

Three-body dynamics in full ephemerides model

In order to explore the effectiveness of different station-keeping methods, the CRTBP explained in Chapter 3 is not sufficiently accurate. The assumptions of circular orbits for the primary bodies are not valid for the real solar system, where the Earth moves around the Sun in an orbit with an eccentricity of 0.017. On top of this eccentricity, several perturbations acting on the spacecraft have to be taken into account. This leads to the need for a more realistic dynamical model, where these assumptions are not made and perturbations are taken into account. The dynamical model used for orbit propagation in the full solar system model will be explained in detail in this chapter. Afterwards, the choices made during the development of the propagator tool will be discussed.

4.1. The Roto-Pulsating Reference Frame

In order to incorporate perturbations and accurate orbits, several possible systems exist.

The most straightforward way would be to use an inertial reference frame centered at the Sun or at the Solar System Barycenter. Using this reference frame would involve very simple equations of motion and could be done accurately if an appropriate scaling in distance and time was used. The biggest downside however to using this inertial reference frame is the complete lack of three-body dynamics. A Halo orbit in an inertial reference frame looks indistinguishable from a normal heliocentric orbit. In order to preserve the dynamics of the three-body problem, this option was discarded.

A second option would be to use a synodic reference frame, where the frame is centered at the Sun and rotates at a constant rate to match the period of the Earth's orbit around the Sun. While three-body dynamics are somewhat preserved in this reference frame, the constant rate of rotation and the fact that the distance between the Sun and the Earth change during an orbit lead to strange behaviours diverging from what one would see in the CRTBP.

Due to the problems inherent in the above-mentioned reference frames the choice was made to use a reference frame that would be a direct translation from the CRTBP to the full ephemerides model. In the chosen reference frame, the center is located in the barycenter of the two primary bodies, the distance between the two bodies is scaled to unity and the reference frame rotates along with the line connecting the two bodies. This is illustrated in Figure 4.1 [1].

The reference frame therefore rotates at a non-uniform rate, and has a changing scaling factor due to the changing distance between the two primaries on elliptical orbits around their barycenter. These two properties – rotation and pulsation – are reflected in the 'Roto-Pulsating' part of the name. The conservation of CRTBP dynamics in this reference frame does come at the cost of it being highly non-inertial, as it is both rotating at a non-uniform rate and pulsating over time. The translation from an inertial reference frame to the RPF and the derivation of the equations of motion in this reference frame are described in the following sections.

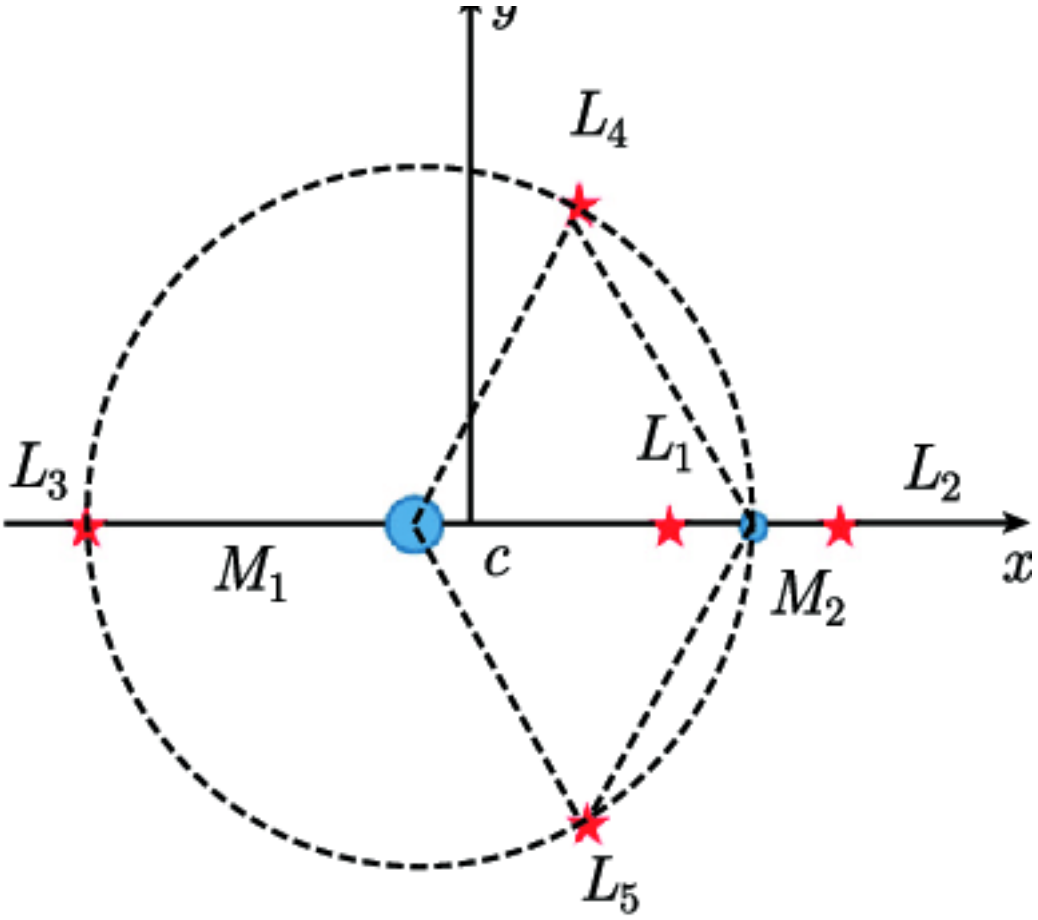

Figure 4.1: The Roto-Pulsating Reference Frame.

4.2. Transformation between reference frames

In order to use accurate ephemerides for the positions of the solar-system bodies considered in the propagation, the transformation between an inertial reference frame and the RPF or vice versa has to be considered. The equation to transform from the RPF to an inertial reference frame is given in Equation (4.1).

$$\bar{R} = \bar{b} + k \cdot C \cdot \bar{\rho} \tag{4.1}$$

In Equation (4.1), $\bar{R}$ is the state in the inertial reference frame, $\bar{\rho}$ is the state in the RPF, the matrix C is a rotation matrix, k is a scalar and corresponds with the distance between the two primary bodies, and $\bar{b}$ is the translation between the center of the inertial reference frame and the center of the RPF.

Before moving on to the definition of the components in Equation (4.1), some properties of the system have to be defined.

$$\begin{aligned} \bar{r} &= \bar{R_S} - \bar{R_P} \\ \bar{v} &= \bar{V_S} - \bar{V_P} \\ \bar{a} &= \bar{A_S} - \bar{A_P} \\ \bar{j} &= \bar{J_S} - \bar{J_P} \\ \bar{s} &= \bar{S_S} - \bar{S_P} \end{aligned} \tag{4.2}$$

where the subscripts S and P denote the secondary and primary bodies, and $\bar{J}$ and $\bar{S}$ represent the jerk and snap, respectively the third and fourth time-derivative of position, $\bar{R}$.

In correspondence with the CRTBP, the translation vector $\bar{b}$ is defined as follows:

$$\bar{b}(t) = \frac{m_P \bar{R}_p + m_S \bar{R}_S}{m_P + m_S} \tag{4.3}$$

The scaling factor k is defined as follows:

$$\begin{aligned} k &= ||\bar{r}|| \\ \dot{k} &= \frac{\bar{r} \cdot \bar{v}}{k} \\ \ddot{k} &= \frac{k(v^2 + \bar{r} \cdot \bar{a}) - \dot{k}(\bar{r} \cdot \bar{v})}{k^2} \end{aligned} \tag{4.4}$$

The angular momentum per unit mass of the system of the two primaries is defined as:

$$\begin{aligned} \bar{h} &= \bar{r} \times \bar{v} \\ h &= ||\bar{h}|| \\ \dot{h} &= \frac{(\bar{r} \times \bar{v}) \cdot (\bar{r} \times \bar{a})}{h} \\ \ddot{h} &= \frac{h\{(\bar{r} \times \bar{a})^2 + (\bar{r} \times \bar{v}) \cdot [\bar{v} \times \bar{a} + \bar{r} \times \bar{j}]\} - \dot{h}(\bar{r} \times \bar{v}) \cdot (\bar{r} \times \bar{a})}{h^2} \end{aligned} \tag{4.5}$$

and the rotation matrix C is defined by the following unit vectors:

$$\begin{aligned} C &= [e_i] \\ \dot{C} &= [\dot{e}_i] \\ \ddot{C} &= [\ddot{e}_i] \end{aligned} \tag{4.6}$$

$$\begin{aligned} e_1 &= \frac{\bar{r}}{k} \\ e_2 &= e_3 \times e_1 \\ e_3 &= \frac{\bar{r} \times \bar{v}}{h} \end{aligned} \tag{4.7}$$

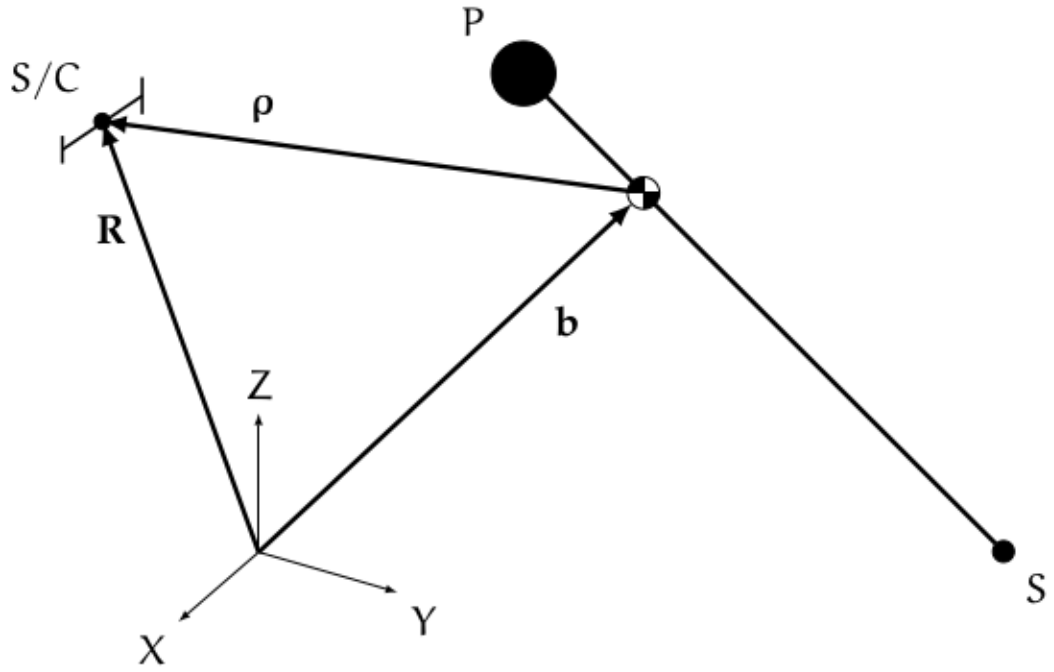

Figure 4.2: Transformation geometry [1]

$$\begin{aligned} \dot{e_1} &= \frac{k\bar{v} - \dot{k}\bar{r}}{k^2} \\ \dot{e_2} &= \dot{e_3} \times e_1 + e_3 \times \dot{e_1} \\ \dot{e_3} &= \frac{h(\bar{r} \times \bar{a}) - \dot{h}(\bar{r} \times \bar{v})}{h^2} \end{aligned} \tag{4.8}$$

$$\begin{aligned} \ddot{e_1} &= \frac{(2\dot{k}^2 - k\ddot{k})\bar{r} - 2k\dot{k}\bar{v} + k^2\bar{a}}{k^3} \\ \ddot{e_2} &= \ddot{e_3} \times e_1 + 2\dot{e_3} \times \dot{e_1} + e_3 \times \ddot{e_1} \\ \ddot{e_3} &= \frac{h^2(\bar{v} \times \bar{a} + \bar{r} \times \bar{j}) - 2h\dot{h}(\bar{r} \times \bar{a}) + (2\dot{h}^2 - h\ddot{h})(\bar{r} \times \bar{v})}{h^3} \end{aligned} \tag{4.9}$$

The geometry of this transformation can be seen in Figure 4.2.

4.3. Equations of Motion

The derivation of the equations of motion is done based on the Lagrangian in the inertial reference frame and its transformation to the RPF. The Lagrangian in the RPF is then used to obtain the set of equations Equation (4.10). The derivation and the definitions for the coefficients is a lengthy process involving the transformation of the Lagrangian of the satellite in the inertial reference frame to the RPF and is described in Appendix B.

$$\begin{aligned} \ddot{x} &= b_1 + b_4\dot{x} + b_5\dot{y} + b_7x + b_9y + b_8z + b_{13}\Omega_{/x} \\ \ddot{y} &= b_2 - b_5\dot{x} + b_4\dot{y} + b_6\dot{z} - b_9x + b_{10}y + b_{11}z + b_{13}\Omega_{/y} \\ \ddot{z} &= b_3 - b_6\dot{y} + b_4\dot{z} + b_8x - b_{11}y + b_{12}z + b_{13}\Omega_{/z} \end{aligned} \tag{4.10}$$

where $\Omega_{/x,y,z}$ is the component of the gradient of the potential of the n-body problem in respectively x, y and z-direction.

4.4. Halo orbit generation in the RPF

In order to analyse station-keeping methods for halo orbits, the initial conditions for halo orbits in the RPF first need to be generated. Because of the lack of extra assumptions such as circular orbits and extra perturbations in the RPF dynamics, a stable halo orbit does not exist in the RPF. Any orbit at the collinear Lagrange points will start to diverge after only a short period of time. The goal is therefore to generate a set of initial conditions that result in a halo orbit that remains stable for as long as possible. The method for orbit generation here is the same as the one implemented in the CRTBP Section 3.3.4. The initial condition resulting from the differential correction scheme in the CRTBP is used in the RPF, leading to an orbit that immediately diverges away from the L2-point. Starting from this bad initial condition, a differential correction scheme is once again used to improve upon the initial guess. After a correction has been made accounting for the first plane-crossing, the procedure is repeated for two more consecutive plane-crossings. More than three plane-crossings was found to be impossible as the instability leads to the orbit inevitably diverging away from a halo orbit before the fourth crossing.

The comparison between the initial conditions taken from the CRTBP and the initial conditions after the differential correction scheme can be seen in Figure 4.3. It is clear that even the corrected initial conditions lead to an orbit that diverges rapidly. This goes to show that the need for effective station-keeping mechanisms is great and in the next chapters, several methods to achieve this will be explored.

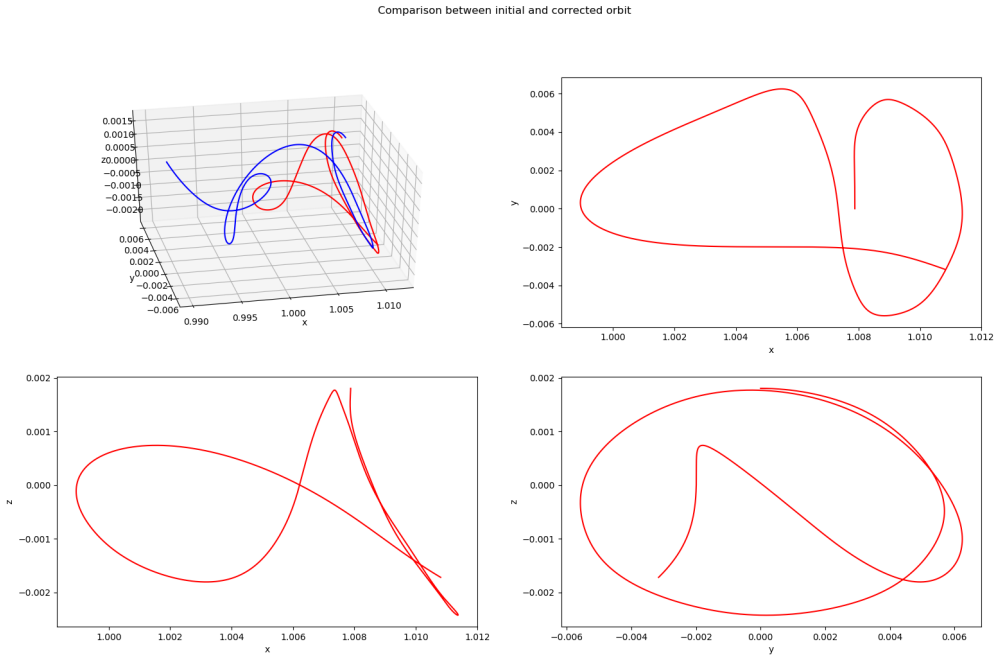

Figure 4.3: Halo orbit in the RPF before (blue) and after differential correction (red).

5 Simulation

In order to later on analyze the performance of various station-keeping methods, a method must first be determined to simulate the dynamics of the spacecraft. For this thesis, two propagators have been built: one for the CRTBP and one for the full dynamics model, including various perturbations.
Both are built upon the SUNDIALS library for numerical integration of ODE's [7]. Both models will be explained here, following by an assessment of the performance of the models and validation against other sources. Finally, the implementation of the halo orbit generation method explained in Section 4.1 will be discussed.

5.1. CRTBP Propagation

In order to generate halo orbits in the full dynamics model, first these orbits are generated in the CRTBP to serve as initial guesses for those in the full model.
The equations of motion of a body in the CRTBP are given in Equation (3.25), which can readily be implemented into a SUNDIALS numerical integrator. For this propagator, the CVODE module of SUNDIALS was chosen. The chosen integration scheme is a variable-timestep, variable-order backwards differentiation formula [7].

5.2. Full dynamics model propagation

In order to simulate a satellite trajectory with realistic perturbations, which are required to accurately estimate the performance of the various station-keeping methods, the satellite state is propagated in the RPF. The equations of motion for the RPF are taken from Section 4.1. The simulation including perturbations from other solar-system bodies and solar radiation pressure (SRP) makes it so that planetary ephemerides are required. For this purpose, the SPICE interface will be used. This library allows for easy access of JPL ephemerides, which contain precise states for most solar-system bodies. The JPL-DE430 ephemerides [4] are used as these are the most recent ones, together with JPL-DE431. The DE431 ephemerides contain data until the year 17191 compared to the year 2650 for the DE430 version. The large size of the DE431 ephemerides disqualifies this for use in the propagator.
The equations of motion for the RPF require knowledge of the relative acceleration and jerk of the two primary bodies. Since the JPL ephemerides only provide position and velocity information, these derivatives are calculated numerically using a first-order central difference scheme.
This leads to some inaccuracies that are inherent in the propagation, but as will be shown later, does not have a significant impact on the performance of the propagator.

5.2.1. Solar Radiation Pressure

For increased accuracy, in the full ephemerides model, the SRP also has to be taken into account. In a Sun-Earth L2 halo orbit, this perturbation is approximately constant in direction. The decision was therefore made to assume that the SRP acceleration always points in the positive x-direction, i.e. straight away from the Sun.
This assumption makes the implementation of SRP simple. The way it is implemented in the simulation is by calculating the magnitude of the acceleration in the inertial reference frame, scaling that magnitude to convert it to the RPF and then applying an acceleration of that magnitude in the positive x-direction in accordance with the above-mentioned assumption.

A solar flux at 1 A.U. distance from the Sun of 1361.1 W/m^2 [17] is used.

5.2.2. Propagator Structure

For simulation purposes, a propagator was constructed in C. The structure of the propagator is outlined in Figure 5.1. The code uses the SUNDIALS library for numerical integration, and the CSPICE library to access the JPL ephemerides. All station-keeping methods described in Part II are implemented and applied after the calculation of the accelerations. Perturbations from all solar system bodies can be individually turned on or off, as well as solar radiation pressure.

The SUNDIALS integrator used is an Adams-Moulton method with maximum order of 12.
The tolerances for the integration depend on the use-case. For simulation purposes, a higher tolerance is used than for optimization. The optimizations that have been done required a higher tolerance to achieve the required levels.

The code can be used to propagate the state alone, or to propagate the state together with the STM. If a station-keeping strategy is selected, the manoeuvres performed are saved in an individual output file, transformed to the inertial reference frame. The satellite parameters that can be changed are the mass, reflectivity coefficient and the effective area for solar radiation pressure.

5.2.3. Validation of the propagator

In order to validate the dynamics implemented in the RPF, the orbit of a Trojan asteroid, i.e. an asteroid orbiting the L4-point of the Sun-Jupiter system, is recreated using the newly generated propagator. 624 Hektor is an asteroid with a mean diameter of 150 km and has ephemerides readily available from JPL. The choice for a Trojan asteroid stems from the inherent stability of L4-orbits. A halo orbit, which is inherently unstable, complicates the validation procedure due to small inaccuracies leading to very large deviations after only a short amount of time.
The asteroid is propagated for a timespan of 28 years and compared against the JPL ephemerides for the same timespan. The result of this comparison can be seen in Figures 5.2 and 5.3.

It can be seen from Figure 5.3 that the dynamics in the RPF are correctly implemented. The deviation is of course still increasing but that can be explained by the inherent inaccuracies in the reference frame transformations and in the higher-order derivatives used in the equations of motion for the RPF. Given the large time span of 28 years, this kind of behaviour is to be expected and the deviation is within reason.

The conclusion is made that the propagator can be considered validated and can safely be used for the analysis further in this thesis.

5.2.4. Halo orbit generation - CRTBP

The differential correction method is implemented in the CRTBP propagator using the STM propagation option. An initial condition is propagated until the next plane crossing is detected, using the event detection tools provided by SUNDIALS, after which the STM is then used to calculate the change in initial conditions required to achieve the desired state at the plane crossing. This change is scaled by 0.1, as the inaccuracies inherent in the propagation make it impossible to achieve the desired change after only one iteration. This procedure is then iteratively repeated until the state at the plane crossing is close enough to the desired state.

5.2.5. Halo orbit generation - full dynamics model

The differential correction for the RPF with full dynamics is implemented in the same way as was done for the CRTBP orbit generation. The main difference is that the Jacobian used for STM propagation is calculated numerically, as opposed to the analytical Jacobian used in the CRTBP. This leads to more inaccuracies, which means that more iterations are required in order for the algorithm to converge.

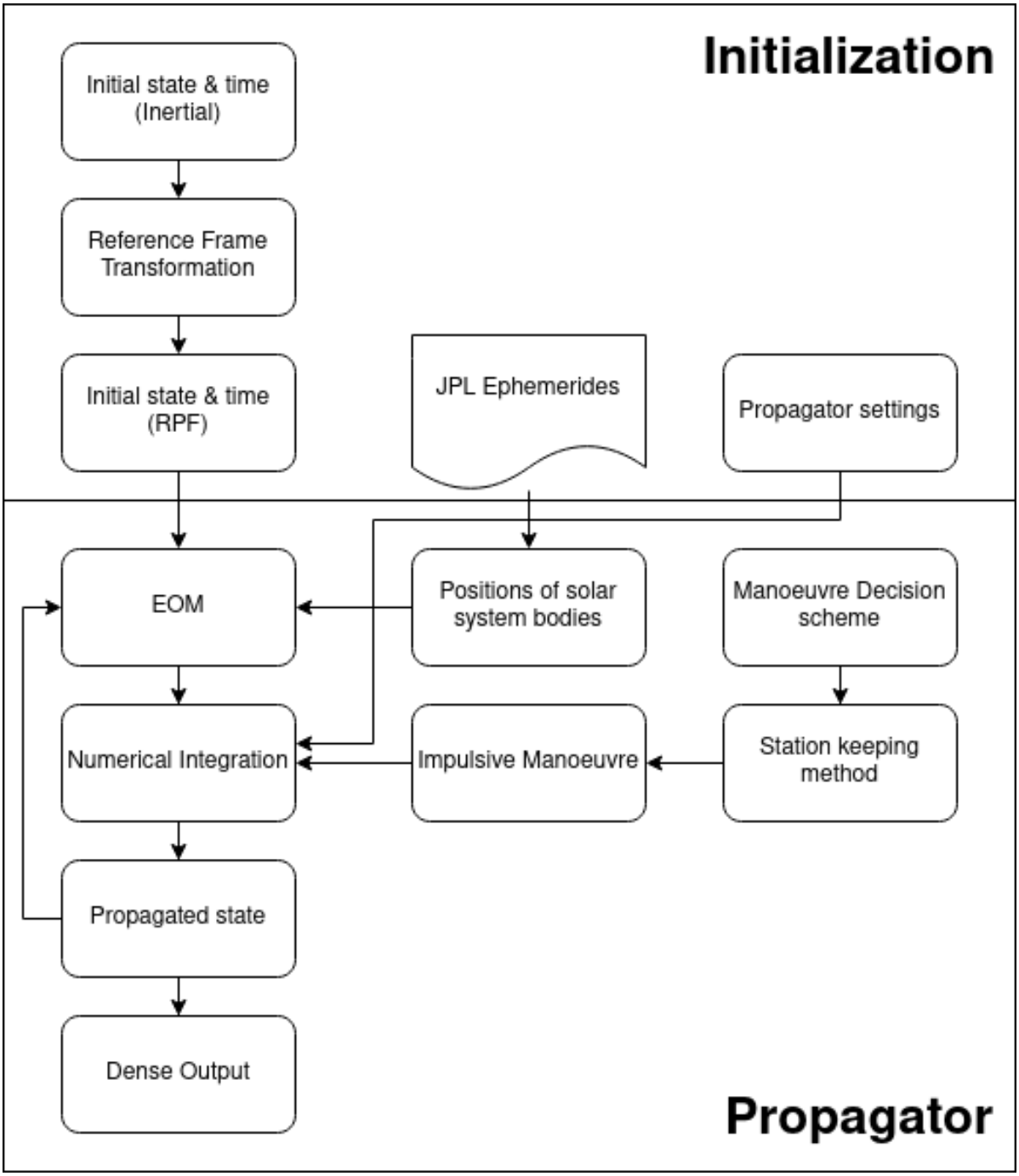

Figure 5.1: Propagator structure

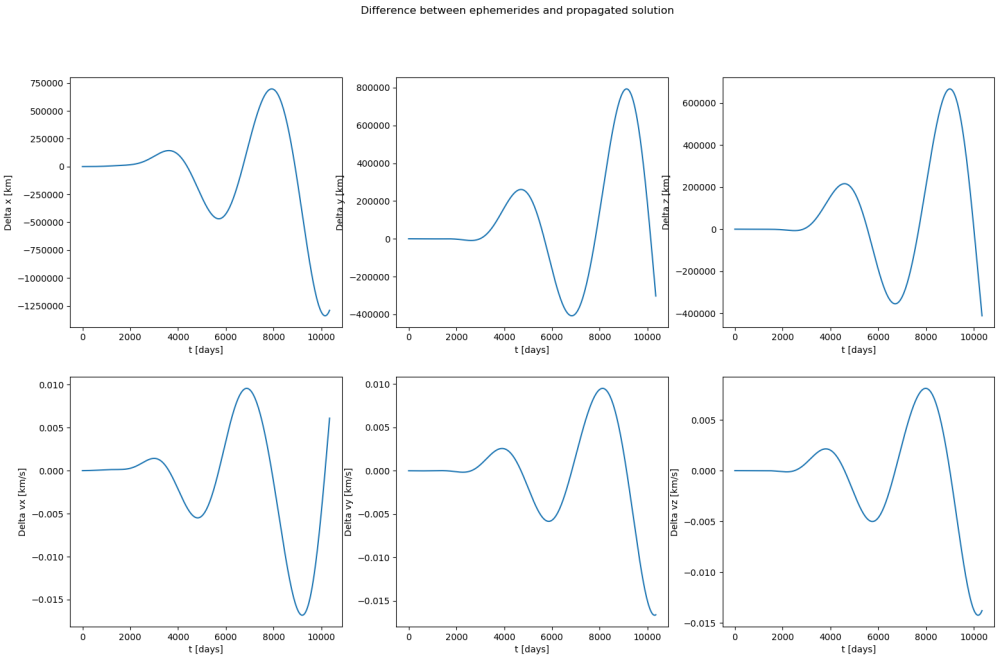

Figure 5.2: Deviations from the JPL ephemerides of Hektor over time (28 years)

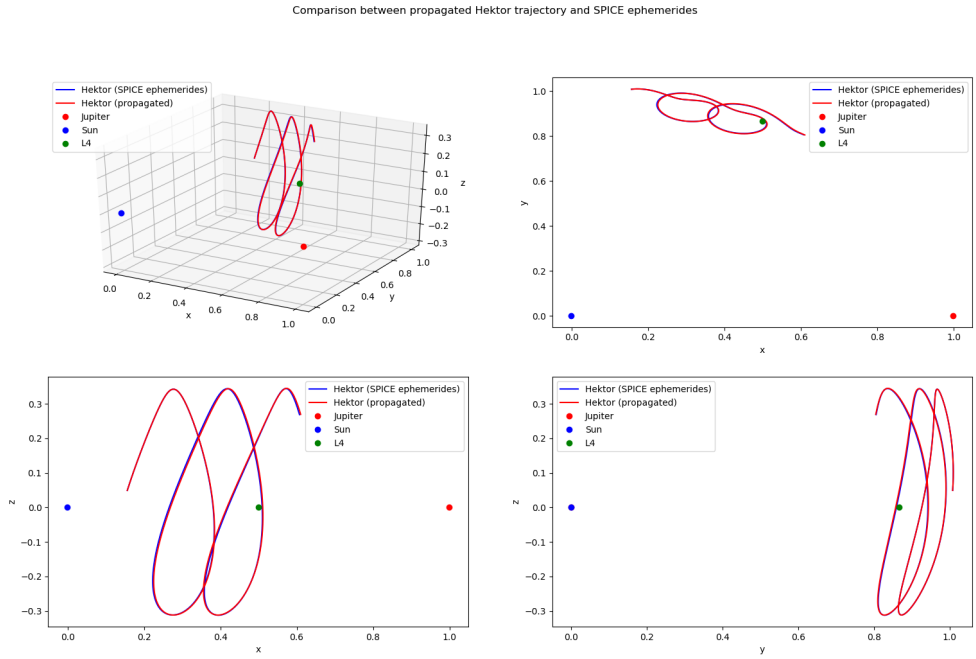

Figure 5.3: Comparison between JPL ephemerides and propagated ephemerides of Hektor in the RPF

The instability of the orbits make it so that correcting for more than two plane crossings in the future is impossible as a stable orbit for such a time span does not exist.

II

Station-keeping strategies in libration-point orbits

In the second part of this thesis, the different station-keeping strategies that were explored for applications in halo orbits are explained. Three different methods were investigated: OCS, DSMC, and FLSMC. The distinction has to be made between the first and the latter two methods. Optimal continuation strategy uses dynamic properties of halo orbits to maintain a stable trajectory, while the sliding mode controllers both make use of a reference orbit to follow. In order to properly evaluate the sliding mode controllers, a method to generate reference orbits was developed.

6

Optimal Continuation Strategy

The first station-keeping method to be implemented was the Optimal Continuation Strategy (OCS) [13]. This method makes use of the state-transition matrix to perform a differential correction, thus calculating an impulsive manoeuvre. The method relies on symmetrical properties of halo orbits in the rotating reference frame.
In an initial representation, a halo orbit crosses the xz-plane with a near-zero velocity in the x-direction. A station-keeping manoeuvre can therefore be calculated using a differential correction scheme, targeting this zero velocity at successive plane-crossings. In actuality the OCS method targets slightly non-zero velocities to push the orbit in the stable direction with every manoeuvre.
For a Southern halo orbit, this means that the target velocity at the upward plane crossing, is slightly positive and the target velocity in the downward plane crossing is slightly negative. This is switched around for a Northern halo orbit.

6.0.1. Differential Correction

As mentioned in the introduction, the OCS mostly relies on differential correction. Differential correction is a method used to calculate the required change in initial condition to achieve a certain target state at a time in the future.

STM Propagation

The required change in state to achieve a stable orbit is calculated using the State-Transition Matrix (STM). the calculation of the STM in the RPF is something that needs to be done numerically. The equations of motion in the RPF are very complex and analytically calculating their derivatives is something beyond the scope of this thesis. Aside from the complexity that would be inherent in using analytical derivatives, these derivatives would include 4th- and 5th-order derivatives of the positions of the two primary bodies with respect to each other. These would have to be calculated numerically, again introducing inaccuracies, and therefore invalidating the extra accuracy resulting from using analytical derivatives.

The STM of a system is defined as follows:

$$\Phi(t, t_0) = \frac{\delta X(t)}{\delta X(t_0)} \tag{6.1}$$

From Equation (6.1), it is clear that $\Phi(t_0, t_0) = I$. This initial condition for the STM will be propagated using the Jacobian.

The Jacobian is the matrix containing all partial derivatives of the equations of motion and is shown in Equation (6.2).
The numerical calculation of the STM is done by numerically calculating the Jacobian of the equations of motion and using that to propagate the STM.

$$J = \begin{bmatrix} \frac{\delta\dot{x}}{\delta x} & \frac{\delta\dot{x}}{\delta y} & \frac{\delta\dot{x}}{\delta z} & \frac{\delta\dot{x}}{\delta\dot{x}} & \frac{\delta\dot{x}}{\delta\dot{y}} & \frac{\delta\dot{x}}{\delta\dot{z}} \\ \frac{\delta\dot{y}}{\delta x} & \frac{\delta\dot{y}}{\delta y} & \frac{\delta\dot{y}}{\delta z} & \frac{\delta\dot{y}}{\delta\dot{x}} & \frac{\delta\dot{y}}{\delta\dot{y}} & \frac{\delta\dot{y}}{\delta\dot{z}} \\ \frac{\delta\dot{z}}{\delta x} & \frac{\delta\dot{z}}{\delta y} & \frac{\delta\dot{z}}{\delta z} & \frac{\delta\dot{z}}{\delta\dot{x}} & \frac{\delta\dot{z}}{\delta\dot{y}} & \frac{\delta\dot{z}}{\delta\dot{z}} \\ \frac{\delta\ddot{x}}{\delta x} & \frac{\delta\ddot{x}}{\delta y} & \frac{\delta\ddot{x}}{\delta z} & \frac{\delta\ddot{x}}{\delta\dot{x}} & \frac{\delta\ddot{x}}{\delta\dot{y}} & \frac{\delta\ddot{x}}{\delta\dot{z}} \\ \frac{\delta\ddot{y}}{\delta x} & \frac{\delta\ddot{y}}{\delta y} & \frac{\delta\ddot{y}}{\delta z} & \frac{\delta\ddot{y}}{\delta\dot{x}} & \frac{\delta\ddot{y}}{\delta\dot{y}} & \frac{\delta\ddot{y}}{\delta\dot{z}} \\ \frac{\delta\ddot{z}}{\delta x} & \frac{\delta\ddot{z}}{\delta y} & \frac{\delta\ddot{z}}{\delta z} & \frac{\delta\ddot{z}}{\delta\dot{x}} & \frac{\delta\ddot{z}}{\delta\dot{y}} & \frac{\delta\ddot{z}}{\delta\dot{z}} \end{bmatrix} \tag{6.2}$$

The Jacobian in Equation (6.2) is calculated numerically using a first-order central difference scheme, varying the state one element at a time and then using the differences in the velocities and accelerations resulting from the equations of motion.

The STM can then be propagated using the Jacobian. The derivative used in this propagation is shown in Equation (6.3).

$$\frac{\delta\Phi(t,t_0)}{\delta t} = J(t)\cdot\Phi(t,t_0) \tag{6.3}$$

The derivative shown in Equation (6.3) can then be used in the same numerical integration scheme that is used for propagation of the state to calculate the STM at any point in time.

Target states

Now that the STM at any point in time can be calculated, the differential correction can be implemented. For this, a set of target states is required. The initial conditions at the time of the manoeuvre are changed to achieve these target states using the STM. The choice of target states is important as this will lead to a stable or unstable orbit.

The properties of a halo orbit are very useful for the determination of these targets. In a halo orbit, the orbit crosses the xz-plane perpendicularly. Therefore, a good initial target would be zero velocities in the x- and z-directions. This works well in the CRTBP but is not sufficient for the RPF, where the extra perturbations push the orbit away from the stable region.

The solution for this is to target slightly non-zero velocities in the x-direction. In this way the orbit is always pushed back towards the region where it is stable.

This can be seen in Figure 6.1, for a northern halo orbit. In this orbit, the velocities targeted at the plane crossings are slightly positive in the southern crossing and slightly negative in the northern crossing.

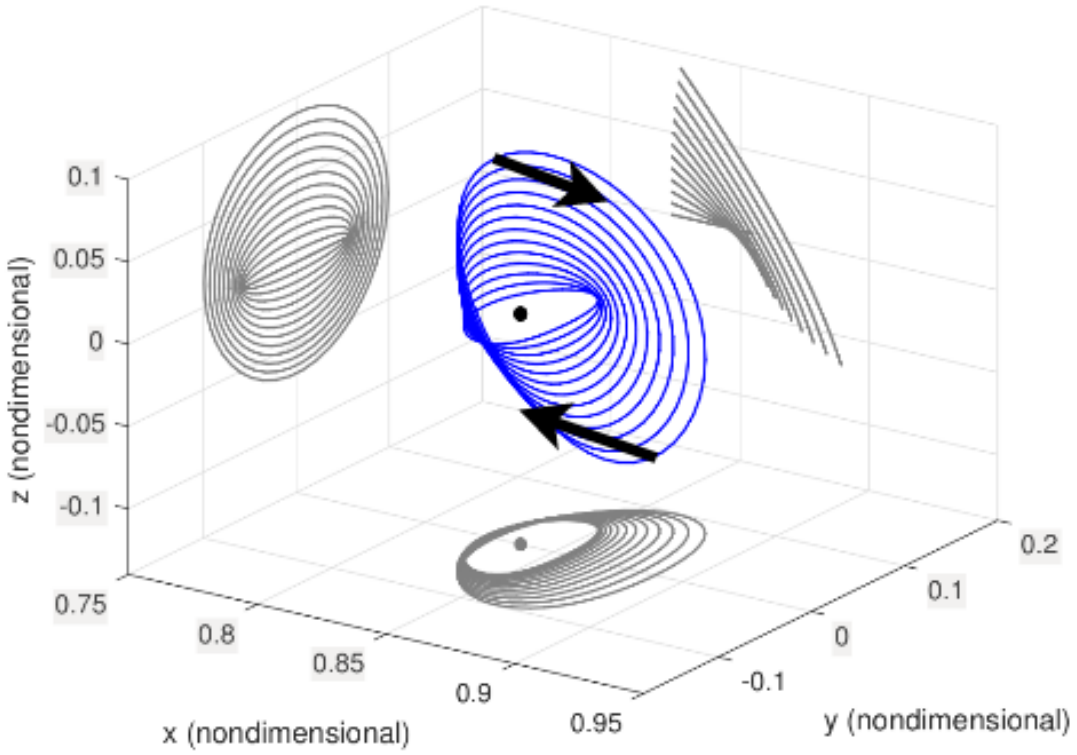

Figure 6.1: Target velocity directions for a northern halo orbit.

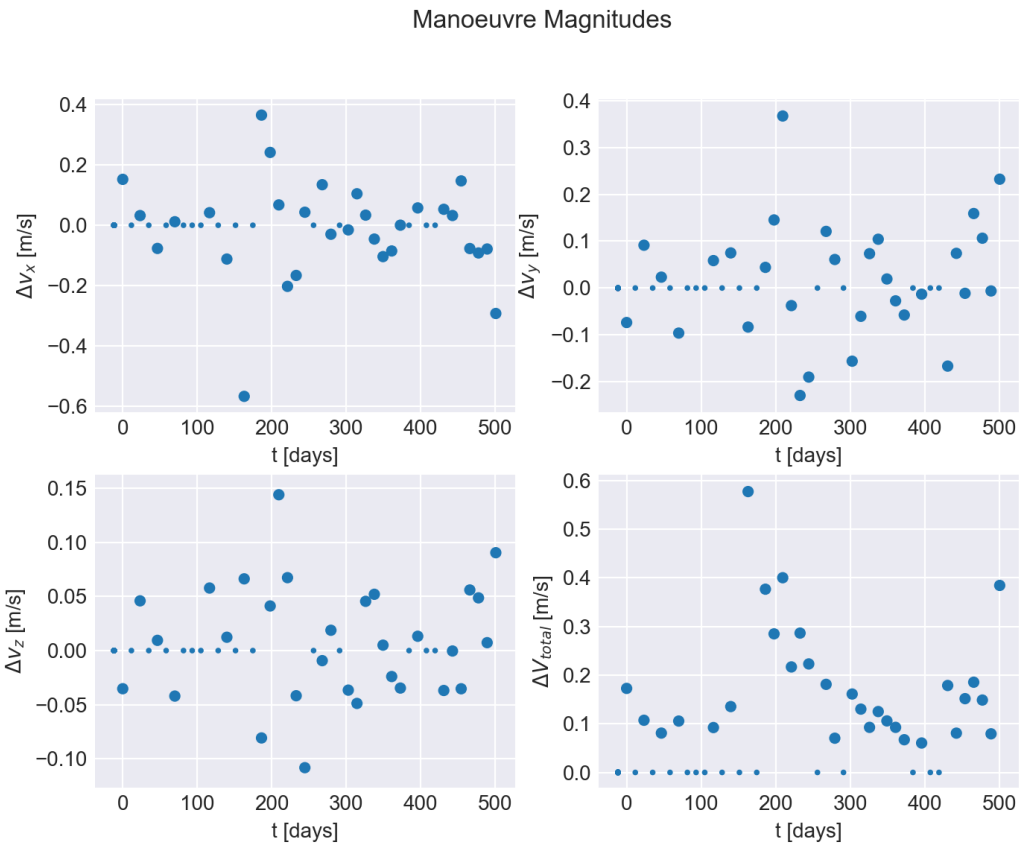

Figure 6.2: Manoeuvre magnitudes for an OCS-controlled halo orbit.

7

Reference Orbit Generation

As was explained at the beginning of this part of the thesis report, the two methods following after OCS, i.e. DSMC and FLSMC, require a reference orbit to follow. This chapter outlines the process of designing such a reference orbit. The quality of the reference orbit has a major impact on the performance of both DSMC and FLSMC and as such, a robust method for creating pseudo periodic halo orbits was required.

7.1. Initial OCS reference orbit

As an initial step, a reference orbit was designed by making use of the OCS method. An orbit was propagated with OCS for the required timespan, with a manoeuvre interval of 0.1 days and no minimum manoeuvre size. The idea behind this was that with such a small interval manoeuvre, the manoeuvres would be sufficiently small such that the orbit could be viewed as almost continuous in position and velocity.
However, it was found that some manoeuvres were still too large, leading to a bad performance of the DSMC and FLSMC methods. The large manoeuvres originated at plane-crossings, where the OCS would start to take into account an extra plane-crossing and would have to perform a large manoeuvre to get this previously unaccounted-for plane-crossing corrected.
This is inherent to the OCS method and makes it unsuitable for use for reference orbit generation.

7.2. Refined multiple-shooting orbit

Due to the shortcomings of the method described above in Section 7.1, another method to generate continuous quasi-periodic halo orbits had to be used. It was decided to use a multiple-shooting method starting with the reference orbit from Section 7.1. The inherent instability of the system makes it so that these quasi-periodic halo orbits are impossible to propagate normally, as any small numerical errors would quickly lead to divergent behaviour and an unstable orbit.
This problem can mostly be solved by using a multiple-shooting method, where the orbit is subdivided into many smaller arcs and the initial conditions of the arcs are tweaked so that the split arcs are patched. By splitting up the orbit into multiple smaller arcs to propagate, the numerical errors can be kept below a certain level and thus the orbit can be made to not diverge.

Using the initial orbit, N points are taken from there and used as initial conditions for the patching method. This leads to $N-1$ arcs that have to be propagated. From each point except for the first and last one, a propagation is done forward and backwards until halfway to the previous or next point, where two arcs will be patched. After all these propagations have been done, the total difference in states at the patch points can be used as a cost-function for an optimization routine. The first point in the orbit will only be propagated forwards, while the last point is only propagated backwards.
A total of N initial points therefore leads to the following cost-function.

$$C = \sum_{i=1}^{N-1} \sqrt{(x_i^{FW} - x_i^{BW})^2 + (y_i^{FW} - y_i^{BW})^2 + (z_i^{FW} - z_i^{BW})^2 + (\dot{x}_i^{FW} - \dot{x}_i^{BW})^2 + (\dot{y}_i^{FW} - \dot{y}_i^{BW})^2 + (\dot{z}_i^{FW} - \dot{z}_i^{BW})^2} \tag{7.1}$$

where the FW and BW subscripts refer to the states obtained by doing a forward or backward propagation.

To perform an efficient optimization, gradients of this cost function had to be obtained first. following from Equation (7.1) and using the STM's that the propagator calculates, the following expressions for the Jacobian of the cost function can be obtained.
In Equation (7.2), the *i* subscript refers to the i-th point in the orbit, where subscript *j* refers to the element of that specific state, i.e. x, y, z, ...

$$J_{i,j} = \sum_{l=1}^{6} \frac{s_{i,l}^{FW} - s_{i,l}^{BW}}{\sqrt{\sum_{k=1}^{6} (s_{i,k}^{FW} - s_{i,k}^{BW})^2}} \cdot STM_{j,l}^{i,FW} + \sum_{l=1}^{6} \frac{s_{i-1,l}^{FW} - s_{i-1,l}^{BW}}{\sqrt{\sum_{k=1}^{6} (s_{i-1,k}^{FW} - s_{i-1,k}^{BW})^2}} \cdot -STM_{j,l}^{i-1,BW} \tag{7.2}$$

Now that the cost function and its gradient have been defined, an optimization can be performed. When using N patch points, a total of $6N$ variables have to be optimized, i.e. 6 for every patch point. The optimization itself is done using IPOPT [16], short for Interior Point Optimizer. As can be seen in Equation (7.2), the Jacobian of the cost function contains a large number of STM terms, which are results from a propagation of an approximated Jacobian. To ensure convergence, the accuracy required from these STM terms is higher than what would be used for a normal propagation. Therefore the propagations being done for the optimization here are done using significantly lower tolerances (10^{-11} instead of 10^{-8}). An example of what the patched orbit looks like, with the patch points marked on it is shown in Figure 7.1.

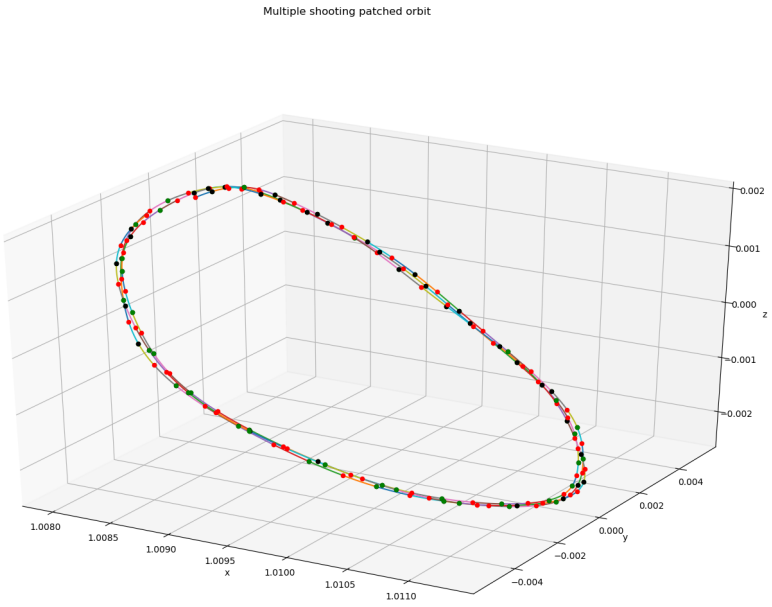

Figure 7.1: A multiple-shooting reference orbit with 24 patch points per revolution.

8

Discrete-time Sliding Mode Control

As a second station-keeping method, the Discrete-time Sliding Mode Controller is introduced. This method, as opposed to the OCS, uses a reference orbit which the satellite has to follow. The design process of this reference orbit has been described in Chapter 7.

Sliding-mode control (SMC) is a non-linear control system for non-linear systems, such as the motion of a satellite in a real solar-system model.
The method aims to move the state of the satellite towards a specific surface in the control state (the nominal orbit) by applying a discontinuous control input to the system such that it slides along this specified surface.
The SMC consists of different control structures, which are linked to subsets of the control space.
The system switches between these control structures in a discontinuous way as it slides along the control surface [11].

8.1. Principles

As a first step in this method, the dynamics with respect to the reference orbit are linearized and discretized using the state transition matrix:

$$x(k+1) = A_d x(k) + B_d \Delta v(k) \tag{8.1}$$

where A_d and B_d are derived from the state transition matrix, and $\Delta v(k)$ is the impulsive manoeuvre applied at epoch t_k. The sliding surface is usually assumed to be linear.

The full procedure for deriving a suitable control law to keep the system's state on the sliding surface is described by Lian et al. [11]. Lian et al. compared the results for the sliding mode control method for station-keeping to a classical Linear Quadratic Regulator for a Halo orbit around the Earth-Moon L2 point and found a significant decrease in required ΔV for the DSMC method. The DSMC method is less sensitive to parameter tuning than an LQR approach but is more sensitive to tracking errors in the position and velocity of the satellite. The exact influence of these errors will be investigated in this thesis using expected tracking errors for upcoming libration point missions.

Sliding Surface Design

Using the sliding surface definition, Equation (8.2), the discrete time equations of motion for the position and velocity deviation, Equation (8.3), and the linear definition of the switching function, Equation (8.4)

$$\sigma = \{\mathbf{x} \in \mathcal{R}^6 | \mathbb{s}(\mathbf{x}) = 0 \in \mathcal{R}^3\} \tag{8.2}$$

$$\begin{aligned} \mathbf{r}(k+1) &= \mathbf{A}_{11}\mathbf{r}(k) + \mathbf{A}_{12}\mathbf{v}(k) \\ \mathbf{v}(k+1) &= \mathbf{A}_{21}\mathbf{r}(k) + \mathbf{A}_{22}\mathbf{v}(k) + \mathbf{B}\Delta\mathbf{v}(k) \end{aligned} \tag{8.3}$$

$$\mathbf{s}(k) = \mathbf{C}\mathbf{x}(k) = \mathbf{C}_1\mathbf{r}(k) + \mathbf{C}_2\mathbf{v}(k) \tag{8.4}$$

we can deduce that, since the state must remain on the sliding surface once it is reached, the following identity must be true.

$$\mathbf{C}_1\mathbf{r}(k) + \mathbf{C}_2\mathbf{v}(k) = 0 \tag{8.5}$$

Consider the performance index

$$J = \sum_{k=0}^{\infty} \left[\mathbf{x}(k)^T \mathbf{Q}\mathbf{x}(k)\right] \tag{8.6}$$

where $\mathbf{Q} = \mathbf{Q}^T$ is the nonsingular positive definite weighting matrix

$$\mathbf{Q} = \begin{bmatrix} \mathbf{Q}_{11} & \mathbf{Q}_{21} \\ \mathbf{Q}_{21} & \mathbf{Q}_{22} \end{bmatrix} \tag{8.7}$$

Introducing a new variable η, representing the nominal control

$$\eta(k) = \mathbf{Q}_{22}^{-1}\mathbf{Q}_{21}\mathbf{r}(k) + \mathbf{v}(k) \tag{8.8}$$

$$\mathbf{r}(k+1) = \mathbf{A}^*\mathbf{r}(k) + \mathbf{A}_{12}\eta(k)$$

$$J = \sum_{k=0}^{\infty} \left[\mathbf{r}^T(k)\mathbf{Q}^*\mathbf{r}(k) + \eta^T(k)\mathbf{Q}_{22}\eta(k)\right] \tag{8.9}$$

where

$$\begin{aligned} \mathbf{A}^* &= \mathbf{A}_{11} - \mathbf{A}_{12}\mathbf{Q}_{22}^{-1}\mathbf{Q}_{21} \\ \mathbf{Q}^* &= \mathbf{Q}_{11} - \mathbf{Q}_{21}\mathbf{Q}_{22}^{-1}\mathbf{Q}_{21} \end{aligned} \tag{8.10}$$

The optimal solution of the system in Equation (8.9) is given by

$$\eta(k) = -\left(\mathbf{Q}_{22} + \mathbf{A}_{12}^T\mathbf{P}\mathbf{A}_{12}\right)^{-1}\mathbf{A}_{12}^T\mathbf{P}\mathbf{A}^* \tag{8.11}$$

where $\mathbf{P}$ is the solution of the following matrix equation

$$\mathbf{P} = \mathbf{Q}^* + \mathbf{A}^{*T}\left[\mathbf{P} - \mathbf{P}\mathbf{A}_{12}(\mathbf{Q}_{22} + \mathbf{A}_{12}^T\mathbf{P}\mathbf{A}_{12})^{-1}\mathbf{A}_{12}^T\mathbf{P}\right]\mathbf{A}^* \tag{8.12}$$

The equation for $\mathbf{P}$ is easily solved iteratively. The expression for $\mathbf{P}$ is stable and thus equating $\mathbf{P}_{i+1} = \mathbf{P}_i$ leads to a converged solution in less than 10 iterations.

Equating Equations 8.8 and 8.11 leads to the following

$$\begin{aligned} \mathbf{C}_1 &= \mathbf{Q}_{21} + \mathbf{Q}_{22}\left(\mathbf{Q}_{22} + A_{12}^T\mathbf{P}\mathbf{A}_{12}\right)^{-1}\mathbf{A}_{12}^T\mathbf{P}\mathbf{A}^* \\ \mathbf{C}_2 &= \mathbf{Q}_{22} \end{aligned} \tag{8.13}$$

Adaptive Control Law Design

As a second step in the design of a sliding-mode controller, an adaptive control law has to be constructed which ensures both the reachability of the sliding surface if the initial state is not on the sliding surface, and the stability of the system once it is on or near the sliding surface [11].

Substituting Equation (8.1) into Equation (8.4), we get

$$\mathbf{s}(k+1) = \mathbf{C}\mathbf{A}\mathbf{x}(k) + \mathbf{C}\mathbf{B}\Delta\mathbf{v}(k) \tag{8.14}$$

The following reaching law will be used:

$$\frac{\mathbf{s}(k+1) - \mathbf{s}(k)}{T} = -\mathbf{D}sgn[\mathbf{s}(k)] - \mathbf{K}\mathbf{s}(k) \tag{8.15}$$

where $T = t_{k+1} - t_k$ is the sampling interval, $\mathbf{D} = diag[\epsilon_1, \epsilon_2, \epsilon_3]$, $\epsilon_i > 0$, $K = diag[k_1, k_2, k_3]$ and $k_i > 0$. This law ensures an exponential approaching speed.

Combining Equations 8.14 and 8.15, and assuming **CB** is nonsingular, we get:

$$\Delta\mathbf{v}(k) = -(\mathbf{CB})^{-1}\{\mathbf{CAx}(k) - (\mathbf{I}_3 - T\mathbf{K})\mathbf{s}(k) + T\mathbf{D}sgn[\mathbf{s}(k)]\} \tag{8.16}$$

where:

$$p_i = 1 - k_i T - \epsilon_i T/[s_i(k)], i = 1, 2, 3 \tag{8.17}$$

Now since $\epsilon_i > 0$, $k_i > 0$ and $T > 0$, we have $p_i < 1$. On top of this we require that $|s_i(k+1)| < |s_i(k)|$, leading to $p_i > -1$. This gives us the following inequalities:

$$\begin{aligned} \epsilon_i &< (2 - k_i T)|s_i(k)|/T \\ i &< 2/T \end{aligned} \tag{8.18}$$

Lian et al. assume in their work a value for ϵ_i and k_i:

$$\begin{aligned} \epsilon_i &= [s_i(k)]/2 \\ k_i &< (4 - T)/(2T) < 2T \end{aligned} \tag{8.19}$$

Equations 8.16 and 8.19 give the definition for the discrete-time sliding mode controller.
During the implementation and testing of the DSMC, it was found that using the manoeuvre interval for the parameter T led to prohibitively large manoeuvres. The inaccuracies inherent in the propagation made targeting a point this far in the future ineffective and led to massive overshooting. A smaller time span T makes it so the DSMC targets a point much closer, which reduces the effect of inaccuracies and leads to more efficient manoeuvres. In the case of perfect accuracy, a larger T would lead to smaller manoeuvres as a small ΔV can drastically change the state when enough time passes.
For the halo orbits considered in the thesis, an interval of 0.05 was used as this led to the lowest ΔV. This corresponds roughly to targeting a point 3 days in the future.

Boundary Layer

In Equation (8.16), the sign function $sgn[\mathbf{s}(k)]$ leads to discontinuous behaviour around the sliding surface. This can be mitigated partially by implementing a so-called boundary layer. The boundary layer is defined as follows:

$$\begin{aligned} BL[\mathbf{s}(k)] &= -1 \quad \text{if } \mathbf{s}(k) < -\frac{l_{BL}}{2} \\ BL[\mathbf{s}(k)] &= -1 + \frac{[\mathbf{s}(k) - \frac{l_{BL}}{2}]}{l_{BL}} \quad \text{if } -\frac{l_{BL}}{2} < \mathbf{s}(k) < \frac{l_{BL}}{2} \\ BL[\mathbf{s}(k)] &= 1 \quad \text{if } \mathbf{s}(k) > \frac{l_{BL}}{2} \end{aligned} \tag{8.20}$$

9

Fuzzy-logic Sliding Mode Control

As a final point in their paper on DSMC for station-keeping in halo orbits, Lian et al. [11] mention the possibility of improvement of their method by combining the DSMC method with fuzzy control. Adding fuzzy control to the control system for station-keeping can help eliminate some of the discontinuous behaviour in the control signal and lead to improved results. This hypothesis will be implemented in the thesis and compared to the traditional DSMC controller, as well as other station-keeping methods.

9.1. Introduction to Fuzzy Logic

Fuzzy logic is a mathematical logic system where the truth value can take on any value between 0 and 1. This is in contrast to boolean logic where something is either true (1) or false (0). The concept of fuzzy logic is used to deal with partially true or partially false. Due to these properties it is often used to more realistically mimic human decision-making processes. [9] A fuzzy control system is a controller that incorporates fuzzy logic in the loop. The general components of such a controller are listed below.

- Membership Functions: Conversions from 'crisp' input values to fuzzy values (between 0 and 1). This process is also known as fuzzification.
- Rule Processor: A number of rules that convert a (set of) fuzzy input value(s) to a (set of) fuzzy output value(s).
- Defuzzifier: Combines the outputs from the rule inference into a (set of) non-fuzzy or crisp output value(s).

For simple control systems, this method can in general be applied quite easily. If we take the case of a heater connected with a thermostat, the input from the thermostat can easily be converted to fuzzy input values for the controller. An example of membership functions that can be used to convert this input temperature to fuzzy values is shown in Figure 9.1.

9.2. Fuzzy Logic Sliding Mode Control

Some of the issues of a Sliding Mode Controller can be mitigated by implementing fuzzy logic. Due to a discontinuous switching function used to switch between control structures, $\mu(s)$, the state will show 'chattering' when it reaches the sliding surface.

$$\begin{aligned} &\mu(s) = 0; \text{at the surface: } s = 0 \\ &\mu(s) = \pm 1; \text{otherwise: } s \neq 0 \end{aligned} \tag{9.1}$$

The idea of Fuzzy Sliding Mode Control (FSMC) is to replace this discontinuous switching function with a fuzzy logic controller. The general concept of fuzzy sliding mode control includes the conversion of the deviation from the sliding surface to a fuzzy variable, which is then processed in the rules processor and then defuzzified to a crisp control signal [2]. In the application for station-keeping, the decision was made to include the rate of change of the deviation as well. The rules can be conceptually stated as shown in Table 9.1.

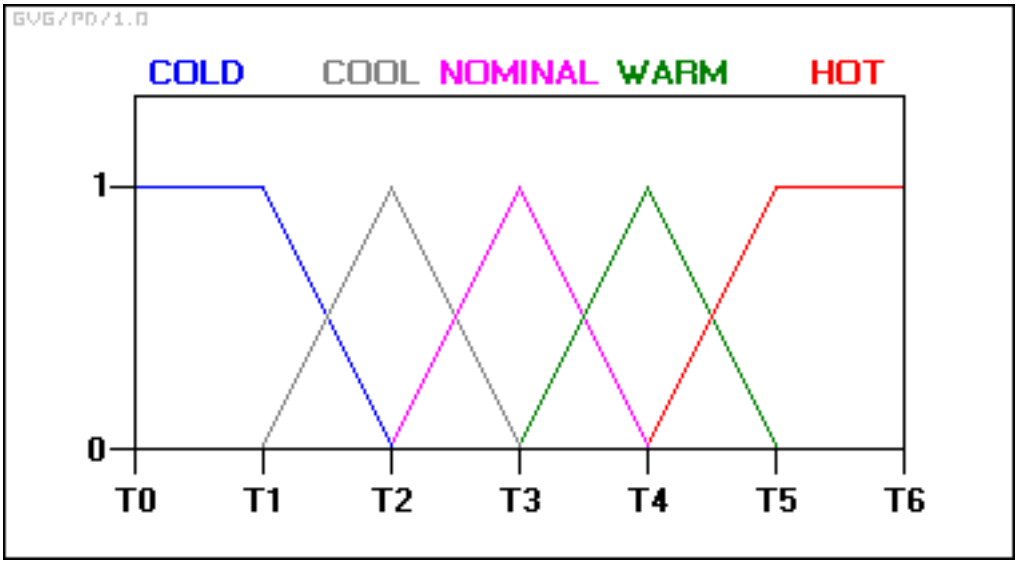

Figure 9.1: Example membership functions for a thermostat controller. Image created by Greg Goebel.

S \ $\dot{S}$	LN	SN	NZ	SP	LP
LN	LP	LP	LP	SP	NZ
SN	LP	SP	SP	NZ	SN
NZ	LP	SP	NZ	SN	LN
SP	SP	NZ	SN	SN	LN
LP	NZ	SN	LN	LN	LN

Table 9.1: Example rules for FLSMC: LN = Large Negative, SN = Small Negative, NZ = Near-Zero, SP = Small Positive, LP = Large Positive

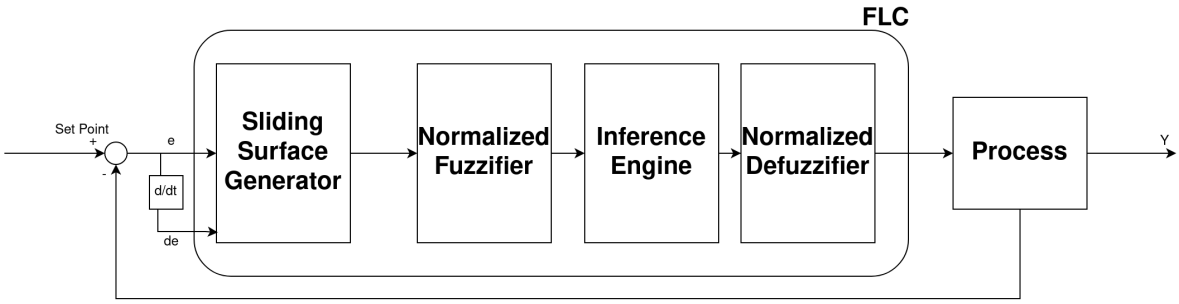

Figure 9.2: Fuzzy Sliding Mode Controller [2].

The structure of an FLSMC is shown in Figure 9.2.

This change from a discontinuous switching function to a fuzzy logic controller deals with the problem of chattering and make the state stay closer to the sliding surface instead of oscillating around it. The concrete implementation of the fuzzy logic switching function uses an output distribution of $[-1, 1]$ in five intervals. For each of the three components of $\mu(S)$, the output value is calculated as follows. At first, the smallest non-zero membership value of both S and $\dot{S}$ is found, which will be called i and j going forward. The weights for the output defuzzification w are calculated as follows:

$$\begin{aligned} w_1 &= min(S[i], \dot{S}[j]) \\ w_2 &= min(S[i+1], \dot{S}[j]) \\ w_3 &= min(S[i], \dot{S}[j+1]) \\ w_4 &= min(S[i+1], \dot{S}[j+1]) \end{aligned} \tag{9.2}$$

The output is then calculated as follows:

$$\mu(S, \dot{S}) = \frac{w_1 u_1 + w_2 u_2 + w_3 u_3 + w_4 u_4}{w_1 + w_2 + w_3 + w_4} \tag{9.3}$$

where:

$$\begin{aligned} u_1 &= (\rho \cdot i + (1-\rho) \cdot j) \cdot D \\ u_2 &= (\rho \cdot (i+1) + (1-\rho) \cdot j) \cdot D \\ u_3 &= (\rho \cdot i + (1-\rho) \cdot (j+1)) \cdot D \\ u_4 &= (\rho \cdot (i+1) + (1-\rho) \cdot (j+1)) \cdot D \end{aligned} \tag{9.4}$$

and $D = \frac{1}{5}$.

The factors ρ are weight factors deciding how much emphasis is put upon S and $\dot{S}$ and are therefore a number between 0 and 1.

After an optimization using NLopt, using a compass-search algorithm [8], the following values were found for the membership limits and the weights ρ by minimizing the total ΔV for a halo orbit for 500 days with the FLSMC.

S_{mid}	S_{high}	$\dot{S}_{mid}$	$\dot{S}_{high}$	ρ_x	ρ_y	ρ_z
$6.9752 \cdot 10^{-5}$	$1.5623 \cdot 10^{-4}$	$3.0305 \cdot 10^{-7}$	$4.2075 \cdot 10^{-5}$	$8.1392 \cdot 10^{-4}$	$1.7255 \cdot 10^{-5}$	$5.5344 \cdot 10^{-1}$

Table 9.2: Parameter values for the optimized FLSMC.

The meaning of the parameters S_{mid}, S_{high}, $\dot{S}_{mid}$ and $\dot{S}_{high}$ is shown in Figure 9.3, where they are shown for S. The principle is exactly the same for $\dot{S}$. The categories are, as explained earlier in this section: large negative, small negative, near zero, small positive and large positive.

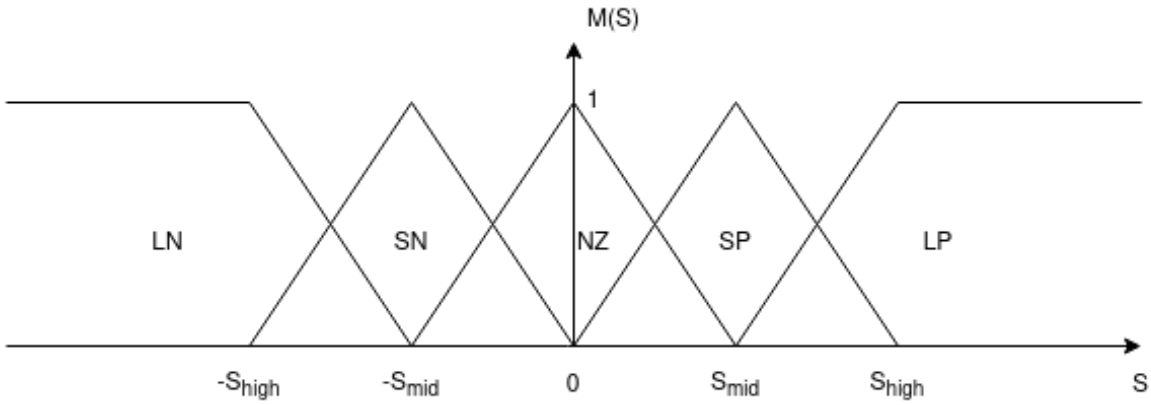

Figure 9.3: Example membership for S. M(S) is the membership for the corresponding category.

10

Analysis of station-keeping methods

Now that all the methods outlined in Part II have been implemented, the comparison between methods can be done. During this comparison, the distinction between OCS and DMSC/FLSMC has to be taken into account. The two types of methods differ in that OCS does not use a reference orbit while the other two methods do.

For each method, a Monte-Carlo analysis was performed with 250 individual simulations. For this Monte-Carlo analysis, a number of uncertainties is taken into account. All of these are taken from a mission currently in design at OHB.

10.1. Monte-Carlo simulation setup

In order to analyze the performance of the station-keeping strategies, their performance when uncertainties are introduced has to be tested. The uncertainties that are used are the following (assumed to follow a Gaussian distribution, all uncertainties mentioned below are 3σ-values):

1. **Position and Velocity:** At the calculation of a manoeuvre, the state has to be known. However, in operation, this state itself is uncertain due to the limitations in orbit determination. An uncertainty is therefore introduced here of a magnitude of 1000 km in position and 0.1 cm/s in velocity.
2. **Manoeuvre execution:** Due to the inaccuracies coming from the thruster, an error is introduced both in manoeuvre magnitude and direction. The uncertainties for these are respectively 0.1% and 0.7 degrees.
3. **Solar radiation pressure:** Due to an unpredictable solar cycle and degradation of the materials of the spacecraft, both the solar flux and the reflectivity coefficient of the spacecraft contain uncertainties. Both flux and reflectivity coefficient are lumped together in one uncertainty of 10%.

The result of the Monte-Carlo analysis is the cumulative ΔV plot of all the runs combined and the distribution of the cumulative ΔV at the end of the run.
All simulations in this chapter have been done for 500 days with manoeuvre interval of 12 days and all of them have the same initial conditions. 500 days was decided to be a long enough period as it already encompassed three revolutions of the halo orbit. An interval of 12 days was chosen since the OCS algorithm started to perform significantly worse for larger intervals.

10.2. OCS

The optimal continuation strategy has been simulated for 250 runs with the uncertainties mentioned above. A manoeuvre interval of 12 days was used and 3 plane-crossings in the future were taken into account.

In Figure 10.1, the result of this simulation can be seen. The effect of passing a plane-crossing can be clearly seen in the regular jumps in ΔV. The period of the nominal halo orbit used in this simulation is around 180 days, meaning that a plane-crossing occurs every 90 days. It can also be noted that the distribution of ΔV is very wide. It appears that the large propagation times necessary for manoeuvre calculation with OCS leads to the uncertainties having a larger impact on the results.

The total ΔV ranges from 3 m/s to 9 m/s. On the right side of Figure 10.1, the distribution of the total ΔV can be seen. Three different lines are marked on the plot, the green line being the simulation where all uncertainties are left out. This means that perfect information is available for the calculation of the manoeuvre. This however does not mean that the calculated ΔV always has to be smaller than in the case where uncertainties are present. The inaccuracies in the STM propagation can still make it so that the uncertainties counteract the error stemming from an inaccurate STM used in manoeuvre calculation.

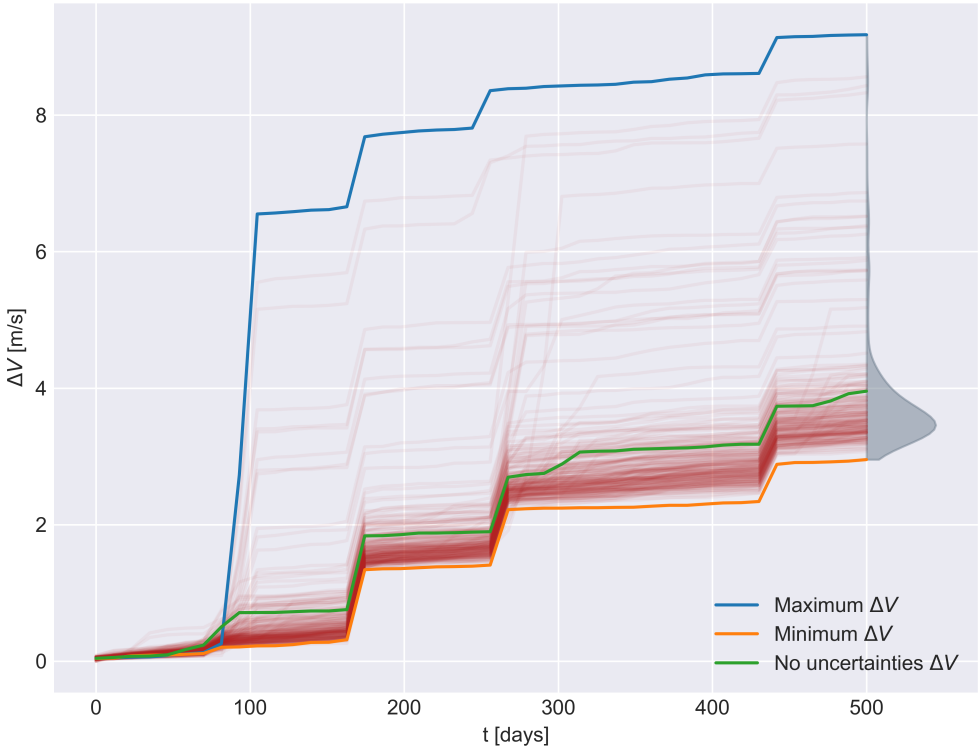

Figure 10.1: Monte-Carlo simulation for optimal continuation strategy: 250 runs.

10.3. DSMC

The Discrete-time Sliding Mode Controller is once again simulated for a period of 500 days and with a manoeuvre interval of 12 days.
The DSMC was first implemented without a boundary layer, for which the results can be seen in Figure 10.2, after which a boundary layer was implemented.

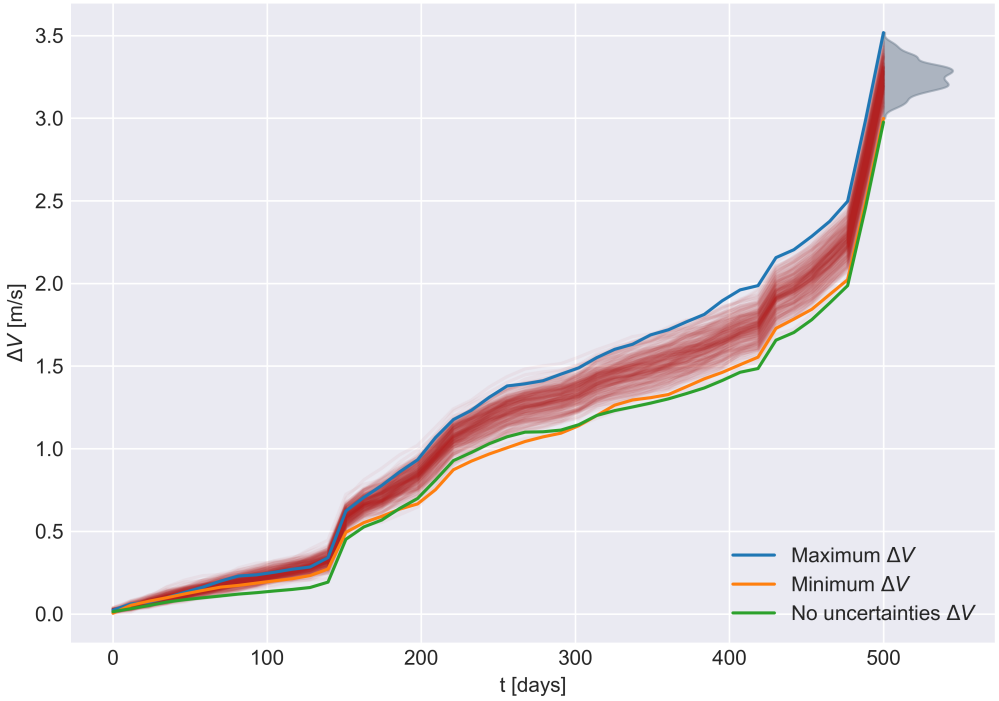

Figure 10.2: Monte-Carlo simulation for DSMC without boundary layer: 250 runs.

The results with the implementation of a boundary layer are shown in Figure 10.3. It can be seen that adding a boundary layer already creates a large improvement over the normal DSMC, with a reduction in mean ΔV of almost 1 m/s. This is mostly because the addition of a boundary layer greatly improves the behaviour of the method when the state is close to the sliding surface.
Due to the gradual change from the boundary layer as opposed to the discontinuous change at the sliding surface when no boundary layer is used, the sliding behaviour is much more smooth, leading to less overshoot and thus smaller total ΔV. The boundary layer width was determined by performing a simple optimization on top of the same parameters used for the DSMC without boundary layer.

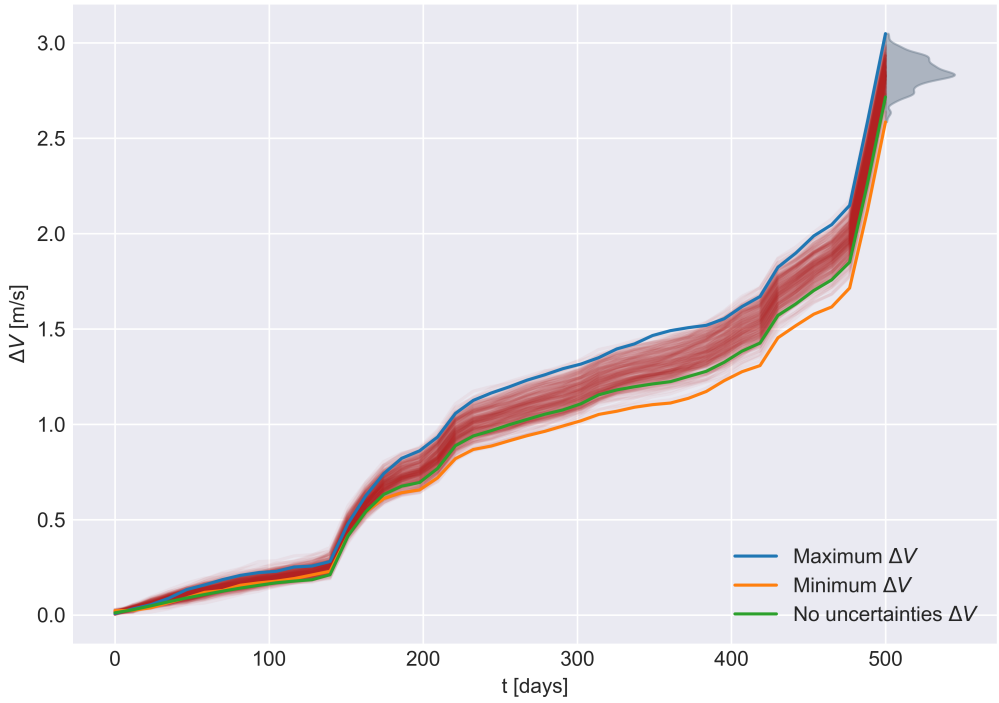

Figure 10.3: Monte-Carlo simulation for DSMC with boundary layer: 250 runs.

As explained in Chapter 8, both DSMC and FLSMC make use of a reference orbit. Despite the best efforts to make this orbit as smooth as possible, the ΔV of this reference orbit is non-zero and therefore it is useful to subtract the effect of the reference orbit ΔV from the results of this Monte-Carlo simulation. This can be seen for the DSMC with boundary layer in Figure 10.4.

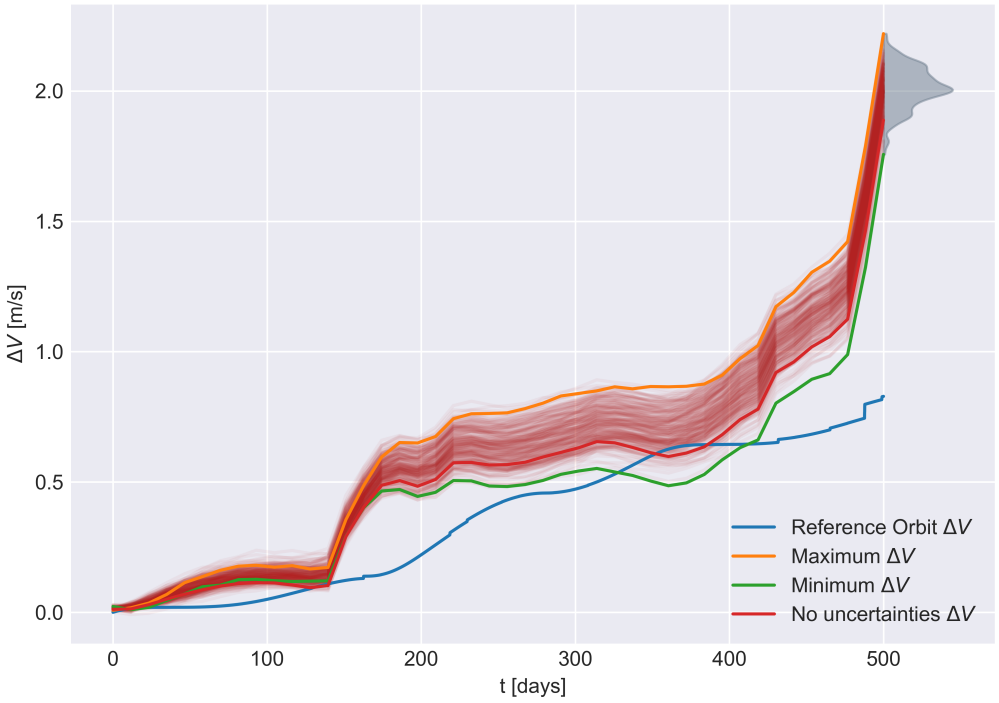

Figure 10.4: Monte-Carlo simulation for DSMC with boundary layer. Reference orbit ΔV shown and subtracted from results.

10.4. FLSMC

As a final method, the Fuzzy-logic sliding mode controller is investigated. This method builds upon the DSMC, but the boundary layer is replaced by a fuzzy logic (FL) function. The FL boundary layer is a function of S and $\dot{S}$, and returns a boundary layer value for both x, y and z components.
The membership functions for S and $\dot{S}$ are determined by performing an optimization using the NLOpt (Non-linear Optimizer) library in C [8]. On top of this, the rules factors ρ_i were optimized to account for different behaviours in the three directions.

After the optimization was performed, the simulation was run under the same circumstances as the previous Monte-Carlo simulations.

It can be seen in Figure 10.5 that the distribution looks similar to the one in Figure 10.3, but has an overall total ΔV that is lower by around 0.3 m/s or around 10%. This shows that the extra complexity introduced by the FL boundary layer provides a significant improvement.

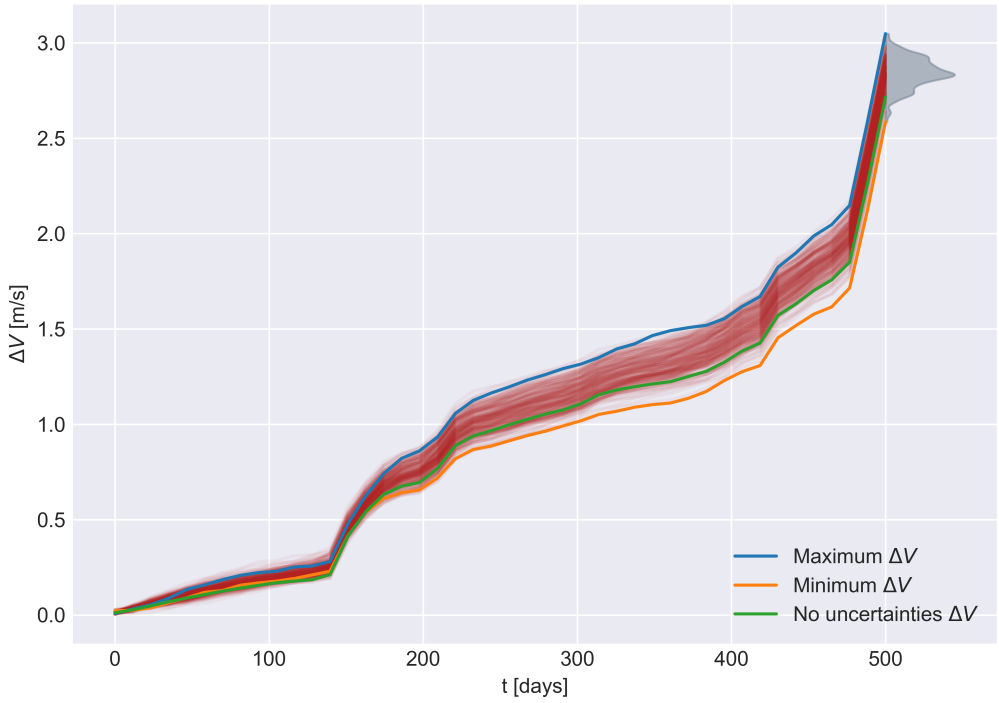

Figure 10.5: Monte-Carlo simulation for FLSMC: 250 runs.

10.5. Comparison

Now that all individual methods have been examined under the same conditions, they can be compared to eachother.
It is clear from Section 10.2 that the OCS has a very high variance and produces overall worse results than both DSMC and FLSMC. As mentioned before, the long propagation times inherent to the OCS make it more susceptible to variance and this is clearly reflected in the results.
The long propagation times also make the algorithm much slower than DSMC and FLSMC, making it an overall worse candidate for station-keeping in this specific application.

10.5.1. Performance comparison

In Figure 10.6, the results for the DSMC with and without boundary layer and the FLSMC are shown together.
This proves that the boundary layer is highly effective in reducing the total ΔV and that improving upon the boundary layer by introducing fuzzy logic leads to another significant, although smaller, improvement.
The sliding mode controllers examined in this chapter therefore are deemed to perform better than OCS, with the FLSMC coming out on top.
Apart from the better results, the SMC methods also are significantly faster than the OCS method, as the manoeuvre calculations typically involve propagations of a few days instead of a year, as is the case for the OCS.
It should be noted that this increased speed does not take into account the reference orbit generation, which is a computationally intensive process, but only has to performed once, after which the reference orbit can be continuously used for testing different station-keeping methods.
It can be concluded from the results aggregated in this chapter, that the sliding mode controllers, al-

though more complex, perform better than OCS and that the addition of a fuzzy logic boundary layer is a useful improvement to the DSMC algorithm and leads to overall better behaviour.

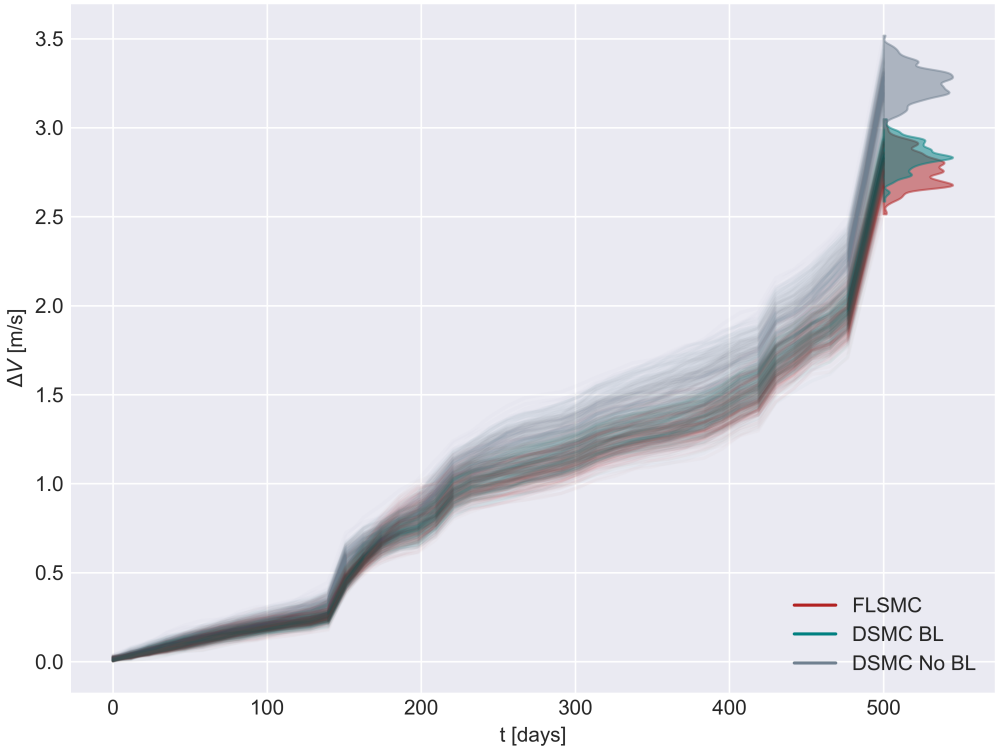

Figure 10.6: Monte-Carlo simulation for DSMC without boundary layer, DSMC with boundary layer and FLSMC: 250 runs.

10.5.2. Uncertainty Quantification

On top of the performance comparisons that have been done in the previous subsection, the impact of the different uncertainties on the performance of the specific methods has been investigated.
The distributions from Figure 10.6 only show the response of the method to the combination of all uncertainties but does not provide any information on the sensitivity to the individual sources of uncertainties.
In order to investigate these properties, an uncertainty quantification is done using a polynomial chaos method.
This is done by fitting a polynomial to the system output, i.e. the total ΔV, with the different errors (see Section 10.1) as inputs.
This polynomial approximation can then be used to quantify the contributions of the different uncertainties to the variance in the final result.
Building a polynomial approximation of the system allows for fast function evaluations. If the relative importance of the different uncertainties would have to be investigated using a Monte-Carlo technique, many different Monte-Carlo simulations with different levels of uncertainties would have to be performed for each method, leading to a prohibitively large number of function evaluations.

Principles
A polynomial chaos (PC) expansion is a non-sampling based method to assess the impact of uncertainties in input parameters to a dynamical system. The benefit of PC over Monte-Carlo is that in general they are computationally faster. This benefit disappears when the number of uncertain input parameters becomes too large, where Monte-Carlo simulations become more efficient again.
For the five uncertain inputs for this evaluation, a PC expansion of the system response is a computationally efficient method for assessing the impact of the different uncertainties.
The specific polynomials being used for PC are in this case Legendre and Hermite Polynomials. The choice for these polynomials stems from the fact that Legendre polynomials are orthogonal with respect to the integral from -1 to 1 and Hermite polynomials are orthogonal with respect to the integral from $-\infty$ to ∞. This makes Legendre polynomials well suited for uniform distributions and Hermite polynomials for gaussian distributions.

The general equation for the polynomial expansion of order N and input uncertainty Ω is shown in Equation (10.1).

$$f(t,\omega) \approx \sum_{n=0}^{N-1} \hat{f}_n(t)\phi_n(\omega) \tag{10.1}$$

where $f(t,\omega)$ is the dynamical system, $\hat{f}_n(t)$ are the weights and $\phi_n(\omega)$ are the polynomials.
The calculation of the weights is done using the python Chaospy library which uses a least-squares method to determine the values for ϕ_n.

Results
After the PC method is used to investigate the response of the different station-keeping methods to the input uncertainties, the results of this analysis can be used to show the relative importance of the different uncertainties. This relative importance can be expressed by the Sobol-coefficients.
These Sobol coefficients are shown in Table 10.1, for each of the methods described in this thesis.

The Sobol indices are a method of variance decomposition that splits up the output variance into fractions that can be attributed to inputs. For d different inputs, the Sobol index for the i-th input variable is defined as follows:

$$V_i = \mathrm{Var}_{X_i}(E_{X_{\approx i}}(Y|X_i)) \tag{10.2}$$

Method	Position	Velocity	SRP	Manoeuvre direction	Manoeuvre Magnitude
OCS	$5.539 \cdot 10^{-1}$	$3.843 \cdot 10^{-2}$	$9.664 \cdot 10^{-2}$	$1.038 \cdot 10^{-16}$	$8.524 \cdot 10^{-1}$
DSMC	$3.612 \cdot 10^{-1}$	$6.167 \cdot 10^{-4}$	$3.190 \cdot 10^{-4}$	$1.960 \cdot 10^{-15}$	$6.375 \cdot 10^{-1}$
FLSMC	$3.046 \cdot 10^{-1}$	$1.029 \cdot 10^{-3}$	$6.591 \cdot 10^{-4}$	$5.925 \cdot 10^{-15}$	$6.929 \cdot 10^{-1}$

Table 10.1: Sobol coefficients for the different station-keeping methods.

From Table 10.1, it is clear that position uncertainty and manoeuvre magnitude error contribute most to the variance in the total ΔV, and the Manoeuvre direction uncertainties contribute significantly less to that variance. While Lian et al. posited in their paper on DSMC for halo orbit station-keeping that the method was particularly sensitive to tracking errors, it can be seen here that this influence is still smaller than it is on the performance of the OCS method. On top of this, the implementation of fuzzy logic brought down this influence slightly.
The orders of magnitude of the Sobol coefficients for all methods are generally similar, meaning that all these methods are roughly equally affected by the different uncertainties relatively.
A notable result from this uncertainty quantification is that the impact of the directional manoeuvre errors is almost negligible for all of the methods. This should be seen within the context of the very small range of possible directional uncertainties. As seen in Section 10.1, the angular error is very small (less than 1 degree) and this uncertainty quantification is only valid within the bounds defined by this range. If the angle was allowed to vary more, the effect of this would be more noticeable.

Bibliography

[1] Diogene Alessandro Dei Tos. *Automated Trajectory Refinement of Three-Body Orbits in the Real Solar System Model*. PhD thesis, Politecnico di Milano, Milan, July 2014.

[2] M. Watheq El-Kharashi and M. A. Sheirah. Tracking Fuzzy Sliding Mode Control. *IFAC Proceedings Volumes*, 30(6):729 – 735, 1997. ISSN 1474-6670. doi: https://doi.org/10.1016/S1474-6670(17)43452-5. URL http://www.sciencedirect.com/science/article/pii/S1474667017434525.

[3] ESA Plato Team. Plato Definition Study Report. Technical Report 1.2, ESA, April 2017.

[4] William M. Folkner, James G. Williams, Dale H. Boggs, Ryan S. Park, and Petr Kuchynka. The Planetary and Lunar Ephemerides DE430 and DE431. IPN Progress Report 42-196, NASA Jet Propulsion Laboratory, February 2014.

[5] Kenneth R. Meyer Glenn R. Hall. *Introduction to Hamiltonian dynamical systems and the n-body problem*. Springer Science+Business Media, New York, NY, 2017. ISBN 978-3-319-53690-3.

[6] Martin Hechler and Arturo Yanez. Herschel/Planck Consolidated Report on Mission Analysis. CREMA PT-MA-RP-0010-OPS-GMA, ESA, January 2006.

[7] Alan C. Hindmarsh, Peter N. Brown, Keith E. Grant, Steven L. Lee, Radu Serban, Dan E. Shumaker, and Carol S. Woodward. SUNDIALS: Suite of nonlinear and differential/algebraic equation solvers. *ACM Transactions on Mathematical Software (TOMS)*, 31(3):363–396, 2005.

[8] Steven G. Johnson. The NLopt nonlinear-optimization package. URL http://github.com/stevengj/nlopt.

[9] Erdal Kayacan and Mojtaba Ahmadieh Khanesar. *Fuzzy Neural Networks For Real Time Control Applications*. Elsevier, 2016.

[10] Wang S. Koon, Martin W. Loo, Jerrold E. Marsden, and Shane D. Ross. *Dynamical Systems, the Three-body Problem and Space Mission Design*. August 2007. URL http://www.cds.caltech.edu/~marsden/volume/missiondesign/KoLoMaRo_DMissionBk.pdf.

[11] Yijun Lian, Gerard Gomez, Josep J. Masdemont, and Guojian Tang. Station-Keeping of Real Earth-Moon Libration Points Using Discrete-time Sliding Mode Control. *Communications in Nonlinear Science and Numerical Simulation*, 19, April 2014. doi: http://dx.doi.org/10.1016/j.cnsns.2014.03.026.

[12] D. L. Richardson. Analytic Construction of Periodic Orbits about the Collinear Points. *Celestial Mechanics*, 22:241–253, October 1980.

[13] Radu Serban, Wang S. Koon, Martin Lo, Jerrold E. Marsden, Linda Petzold, Shane Ross, and Roby S. Wilson. Halo orbit mission correction maneuvers using optimal control. *Automatica*, 38: 571 – 583, April 2002. doi: 10.1016/S0005-1098(01)00279-5.

[14] Maksim Shirobokov, Sergey Trofimov, and Makhail Ovchinnikov. Survey of Station-Keeping Techniques for Libration Point Orbits. *Journal of Guidance, Control and Dynamics*, 40(5), May 2017. doi: https://doi.org/10.2514/1.G001850.

[15] Kiarash Tajdaran. *Incorporations of Mission Design Constraints in Floquet Mode and Hamiltonian Structure-Preserving Orbital Maintenance Strategies for Libration Point Orbits*. PhD thesis, Purdue University, West Lafayette, Indiana, December 2015.

[16] A. Wachter and L.T. Biegler. On the implementation of a primal-dual interior point filter line search algorithm for large-scale nonlinear programming. *Mathematical Programming*, 106(1): 25–57, 2006.

[17] James Wertz. Mission geometry: orbit and constellation design and management: spacecraft orbit and attitude systems. 01 2001.

A

Third-order Richardson expansion

In this appendix, the expressions for the coefficients in Equation (3.44) are given.

$$
\begin{aligned}
a_{21} &= \frac{3c_3(k^2-2}{4(1+2c_2} \\
a_{22} &= \frac{3c_3}{4(1+2c_2)} \\
a_{23} &= -\frac{3c_3\lambda}{4kd_1}[3k^3\lambda - 6k(k-\lambda)+4] \\
a_{24} &= -\frac{3c_3\lambda}{4kd_1}(2+3k\lambda) \\
a_{31} &= -\frac{9\lambda}{4d_2}[4c_3(ka_{23}-b_{21}) + kc_4(4+k^2)] \\
&\quad + (\frac{9\lambda^2+1-c_2}{2d_2})[3c_3(2a_{23}-kb_{21}) + c_4(2+3k^2)] \\
a_{32} &= -\frac{1}{d^2}\{\frac{9\lambda}{4}[4c_3(ka_{24}-b_{22}) + kc_4] \\
&\quad + \frac{3}{2}(9\lambda^2+1-c_2)[c_3(kb_{22}+d_{21}-2a_{24}) - c_4]\} \\
b_{21} &= -\frac{3c_3\lambda}{2d_1}(3k\lambda - 4) \\
b_{22} &= \frac{3c_3\lambda}{d_1} \\
b_{31} &= \frac{3}{8d_2}\{8\lambda[3c_3(kb_{21}-2a_{23}) - c_4(2+3k^2)] \\
&\quad + (9\lambda^2+1+2c_2)[4c_3(ka_{23}-b_{21}) + kc_4(4+k^2)]\} \\
b_{32} &= \frac{1}{d^2}\{9\lambda[c_3(kb_{22}+d_{21}-2a_{24}) - c_4] \\
&\quad + \frac{3}{8}(9\lambda^2+1+2c_2)[4c_3(ka_{24}-b_{22}) + kc_4]\} \\
d_{21} &= -\frac{c_3}{2\lambda^2} \\
d_{31} &= \frac{3}{64\lambda^2}(4c_3a_{24}+c_4) \\
d_{32} &= \frac{3}{64\lambda^2}[4c_3(a_{23}-d_{21}) + c_4(4+k^2)]
\end{aligned}
\tag{A.1}
$$

B

The Roto-Pulsating Reference Frame

In this appendix, the detailed derivation of the equations of motion for the RPF and the definitions of the coefficients of Equation (4.10) are given.
The derivation of these equations is taken from [1].

The geometry of the RPF is seen in Figure B.1.

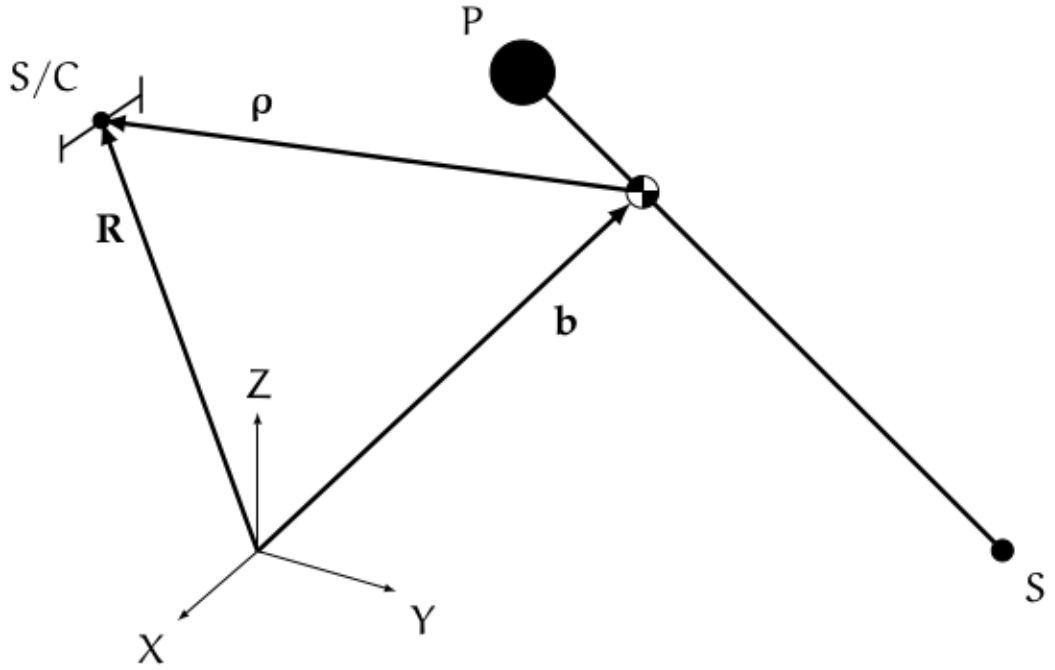

Figure B.1: Transformation Geometry of the three-body problem from an inertial reference frame [1]

The transformation between the solar system barycentric reference frame, SSB and the RPF is:

$$R = b + kC\rho \tag{B.1}$$

where:

$$\begin{aligned} b(t) &= \frac{m_P R_P + m_S R_S}{m_P + m_S} \\ k &= k(t) \\ C &= C(t) \end{aligned} \tag{B.2}$$

The subscripts P and S refer to the primary and secondary body. The translation from the RPF centre to the SSB centre is given by b. The rotation is handled by the cosine angle matrix, C and the scaling is done using a constant time-dependent factor $k(t)$.

In the RPF, the positions and velocities of the two primaries are given by:

$$\begin{aligned} \rho_P &= (-\mu, 0, 0)^T \\ \dot{\rho_P} &= 0 \\ \rho_S &= (1-\mu, 0, 0)^T \\ \dot{\rho_S} &= 0 \end{aligned} \tag{B.3}$$

The following relative vectors will be used in the derivation of the equations of motion:

$$\begin{aligned} r &= R_S - R_P \\ v &= V_S - V_P \\ a &= A_S - A_P \\ j &= J_S - J_P \\ s &= S_S - S_P \end{aligned} \tag{B.4}$$

where J and S are the jerk and the snap, respectively the third and fourth-order time-derivative of R.

The scaling factor k and its' time-derivatives are defined as follows:

$$\begin{aligned} k &= ||r|| \\ \dot{k} &= \frac{r \cdot v}{k} \\ \ddot{k} &= \frac{k(v^2 + r \cdot a) - k(\dot{r} \cdot v}{k^2} \end{aligned} \tag{B.5}$$

The angular momentum, $h = r \times v$ and its' time-derivatives are defined as:

$$\begin{aligned} \bar{h} &= r \times v \\ h &= ||h|| \\ \dot{h} &= \frac{(r \times v) \cdot (r \times a)}{h} \\ \ddot{h} &= \frac{h\{(r \times a)^2 + (r \times v) \cdot [v \times a + r \times j]\} - \dot{h}(r \times v) \cdot (r \times a)}{h^2} \end{aligned} \tag{B.6}$$

The unit vectors in the cosine angle matrix C, $e_i, i = 1, 2, 3$ are defined as:

$$\begin{aligned} C &= [e_i] \\ \dot{C} &= [\dot{e_i}] \\ \ddot{C} &= [\ddot{e_i}] \end{aligned} \tag{B.7}$$

$$\begin{aligned} e_1 &= \frac{r}{k} \\ e_2 &= e_3 \times e_1 \\ e_3 &= \frac{r \times v}{h} \end{aligned} \tag{B.8}$$

$$\begin{aligned} \dot{e_1} &= \frac{kv - \dot{k}r}{k^2} \\ \dot{e_2} &= \dot{e_3} \times e_1 + e_3 \times \dot{e_1} \\ \dot{e_3} &= \frac{h(r \times a) - \dot{h}(r \times v)}{h^2} \end{aligned} \tag{B.9}$$

$$\begin{aligned}\ddot{e_1} &= \frac{(2\dot{k}^2 - k\ddot{k})r - 2k\dot{k}v + k^2 a}{k^3} \\ \ddot{e_2} &= \ddot{e_3} \times e_1 + 2\dot{e_3} \times \dot{e_1} + e_3 \times \ddot{e_1} \\ \ddot{e_3} &= \frac{h^2(v \times a + r \times j) - 2h\dot{h}(r \times a) + (2\dot{h}^2 - h\ddot{h})(r \times v)}{h^3}\end{aligned} \tag{B.10}$$

B.1. Derivation of the equations of motion

The Lagrangian of the system, defined in the SSB reference frame is given by:

$$L(R, \dot{R}, t) = T - V = \frac{1}{2}\dot{R} \cdot \dot{R} + \sum_{j \in S} \frac{Gm_j}{||R - R_j||} \tag{B.11}$$

Where G is the universal constant of gravitation, S is the set of all celestial bodies included in the simulation, and m_j is the mass of a body in that set.
The derivation of the equations of motion in the RPF will be done by transforming the Lagrangian to the RPF and then getting the EOM from there.
As a final preparation, the time adimensionalization is taken care of. The time will be adimensionalized with respect to the rotational velocity of the primary and secondary bodies with respect to their centre of mass. The transformation is then:

$$\tau = \omega \cdot (t - t_0) \tag{B.12}$$

and the differentiation with respect to τ is done as follows:

$$\begin{aligned}\frac{d}{dt} &= \dot{\tau}\frac{d}{d\tau} \\ \frac{d^2}{dt} &= \dot{\tau}^2\frac{d^2}{d\tau^2} + \ddot{\tau}\frac{d}{d\tau}\end{aligned} \tag{B.13}$$

where $\dot{\tau} = \dot{\omega} \cdot (t - t_0)$ and $\ddot{\tau} = \ddot{\omega}(t - t_0) + 2\dot{\omega}$.

In order to calculate the kinetic energy V in the lagrangian, the velocity of the spacecraft in the RPF has to be known. This is done by deriving Equation (B.1).

$$\dot{R} = \dot{b} + \dot{k}C\rho + k\dot{C}\rho + kC\dot{\rho} \tag{B.14}$$

Using the chain rule Equation (B.13), the kinetic and potential energies in the RPF can be calculated as follows:

$$\begin{aligned}T &= \frac{\dot{\tau}^2}{2}(b' + k'C\rho + kC'\rho + kC\rho')^T(b' + k'C\rho + kC'\rho + kC\rho') \\ &= \frac{\dot{\tau}^2}{2}(b'^T b' + k'^2\rho^T\rho + k^2\rho^T C'^T C'\rho + k^2\rho'^T\rho' + 2k'b'^T C\rho \\ &+ 2kb'^T C'\rho + 2kb'^T C\rho' + 2kk'\rho^T C^T C'\rho + 2kk'\rho^T\rho' \\ &+ 2k^2\rho^T C'^T C\rho')\end{aligned} \tag{B.15}$$

$$V = -\sum j \in S\frac{\mu_j}{k||C(\rho - \rho_j||} = \frac{\mu_P + \mu_S}{k}\Omega \tag{B.16}$$

where Ω is the auxiliary potential for the n-body problem, μ_P and μ_S are the mass parameters for the primary and secondary, i.e. $\mu_{P,S} = Gm_{P,S}$.

$$\Omega = -(\frac{1 - \mu}{||\rho - \rho_P||} + \frac{\mu}{||\rho - \rho_S||} + \sum_{j \in S^*}\frac{\hat{\mu}_j}{||\rho - \rho_j||}) \tag{B.17}$$

Where S^* is the set of celestial bodies in the n-body problem, excluding the primary and secondary body and $\hat{\mu}_j = m_j/(m_S + m_P)$.

Then we can write the lagrangian in the RPF as follows:

$$L(\rho, \rho', \tau) = T(\rho, \rho', \tau) + \frac{\mu_P + \mu_S}{k}\Omega(\rho, \tau, \{\mu\}_j) \tag{B.18}$$

We can then use the following relation to derive the equations of motion:

$$\frac{d}{d\tau}\left(\frac{\delta L}{\delta \rho'^T}\right) - \frac{\delta L}{\delta \rho^T} = Q = 0 \tag{B.19}$$

The component of the active forces Q is supposed to be zero since perturbations are neglected in this formulation.
The partial derivatives needed for the derivation are given by:

$$\frac{\delta L}{\delta \rho'^T} = \frac{\delta T}{\delta \rho'^T} = \dot{\tau}^2(k^2\rho' + kC^T b' + kk'\rho + k^2 C^T C'\rho) \tag{B.20}$$

$$\begin{aligned}\frac{d}{d\tau}\left(\frac{\delta L}{\delta \rho'^T}\right) = \frac{d}{d\tau}\left(\frac{\delta T}{\delta \rho'^T}\right) = 2\ddot{\tau}(k^2\rho' + kC^T b' + kk'\rho + k^2 C^T C'\rho) \\ +\dot{\tau}^2(2kk'\rho' + k^2\rho'' + k'C^T b' + kC'^T b' + kC^T b'' \\ +k'^2\rho + kk''\rho + kk'\rho' + 2kk'C^T C'\rho + k^2 C'^T C'\rho \\ +k^2 C^T C''\rho + k^2 C^T C'\rho')\end{aligned} \tag{B.21}$$

$$\begin{aligned}\frac{\delta L}{\delta \rho^T} = \dot{\tau}^2[k'^2\rho + k^2 C'^T C'\rho + k'C^T b' + kC'^T b' + kk'(C^T C' + C'^T C) \\ + kk'\rho' + k^2 C'^T C\rho'] + \frac{\mu_P + \mu_S}{k}\nabla\Omega\end{aligned} \tag{B.22}$$

$$\nabla\Omega = \frac{\delta\Omega}{\delta\rho^T} = (1-\mu)\frac{\rho - \rho_P}{||\rho - \rho_P||^2} + \mu\frac{\rho - \rho_S}{||\rho - \rho_S||^3} + \sum_{j\in S^*}\hat{\mu}_j\frac{\rho - \rho_j}{||\rho - \rho_j||^3} \tag{B.23}$$

Finally, summing and simplifying:

$$\begin{aligned}\rho'' + 2\left(\frac{\ddot{\tau}}{\dot{\tau}^2} + \frac{k'}{k} + C^T C'\right)\rho' + \left[2\frac{\ddot{\tau}}{\dot{\tau}^2}\left(\frac{k'}{k} + C^T C'\right) + \frac{k''}{k}\right. \\ \left. +2\frac{k'}{k}C^T C' + C^T C''\right]\rho + 2\frac{\ddot{\tau}}{\dot{\tau}^2}\frac{1}{k}C^T b' + \frac{1}{k}C^T b'' = \frac{\mu_P + \mu_S}{\dot{\tau}^2 k^3}\nabla\Omega\end{aligned} \tag{B.24}$$

Now that we have the expression for ρ'', the equations of motion can finally be written in the form:

$$x' = f(\tau, x) \tag{B.25}$$

where:

$$\begin{aligned}x &= \begin{bmatrix}\rho \\ \rho'\end{bmatrix} \\ f(\tau, x) &= \begin{bmatrix}\rho' \\ \rho''\end{bmatrix}\end{aligned} \tag{B.26}$$

B.2. Coefficients for EOM in the RPF

In Section 4.1, the expression for the equations of motion is given. The coefficients in Equation (4.10) are given in this section.

$$\begin{aligned}\ddot{x} &= b_1 + b_4\dot{x} + b_5\dot{y} + b_7 x + b_9 y + b_8 z + b_{13}\Omega_{/x} \\ \ddot{y} &= b_2 - b_5\dot{x} + b_4\dot{y} + b_6\dot{z} - b_9 x + b_{10} y + b_{11} z + b_{13}\Omega_{/y} \\ \ddot{z} &= b_3 - b_6\dot{y} + b_4\dot{z} + b_8 x - b_{11} y + b_{12} z + b_{13}\Omega_{/z}\end{aligned} \tag{B.27}$$

$$\begin{aligned}b_1 &= -\frac{\ddot{b}\cdot e_1}{kn^2} \\ b_2 &= -\frac{\ddot{b}\cdot e_2}{kn^2} \\ b_3 &= -\frac{\ddot{b}\cdot e_3}{kn^2} \\ b_4 &= -\frac{2}{n}\frac{\dot{k}}{k} \\ b_5 &= \frac{2}{n} e_2\cdot\dot{e}_1 \\ b_6 &= \frac{2}{n} e_3\cdot\dot{e}_2 \\ b_7 &= -\frac{1}{n^2}\left(\frac{\ddot{k}}{k} - \dot{e}_1\cdot\dot{e}_1\right) \\ b_8 &= \frac{1}{n^2}\dot{e}_1\cdot\dot{e}_3 \\ b_9 &= \frac{1}{n^2}\left(2\frac{\dot{k}}{k}e_2\cdot\dot{e}_1 + e_2\cdot\ddot{e}_1\right) \\ b_{10} &= -\frac{1}{n^2}\left(\frac{\ddot{k}}{k} - \dot{e}_2\cdot\dot{e}_2\right) \\ b_{11} &= \frac{1}{n^2}\left(2\frac{\dot{k}}{k}e_3\cdot\dot{e}_2 + e_3\cdot\ddot{e}_2\right) \\ b_{12} &= -\frac{1}{n^2}\left(\frac{\ddot{k}}{k} - \dot{e}_3\cdot\dot{e}_3\right) \\ b_{13} &= \frac{\mu_S + \mu_P}{k^3 n^2}\end{aligned} \tag{B.28}$$